Investigation of the Turbulent Flow beneath an Ice Block using Particle Image Velocimetry

by

Tanzim Ahmed

A thesis submitted to the Faculty of Graduate Studies of
The University of Manitoba
in partial fulfillment of the requirements of the degree of

Master of Science

Department of Civil Engineering
University of Manitoba
Winnipeg, Manitoba
Canada

Copyright © 2020 by Tanzim Ahmed

ABSTRACT

Transported ice blocks can contribute to the development of river ice jams leading to flooding, which has social, economic and ecological impacts on different parts of the northern hemisphere. The moving ice blocks can either be entrained into the flow or halted by an intact ice cover. Understanding the flow physics beneath an ice block is critical for understanding the stability of ice blocks, which is important for river ice jam development and the design of river ice control works. The present study used particle image velocimetry to analyze the flow field beneath an ice block. A 0.025 m thick rectangular acrylic sheet was used to simulate an ice block and detailed velocity measurements conducted beneath it for various approach Froude number and thickness-to-depth ratios (t/h). The flow field in the recirculation, reattachment regions and some selected locations after the reattachment beneath the block were evaluated.

Results showed that, the higher the Froude number and t/h ratio, the greater the flow separation at the leading edge of the block resulting in greater reattachment length beneath the ice block. This is important, as it is known that flow separation at the leading edge causes a pressure reduction that can destabilize the blocks. The mean velocity profile, the turbulence intensity profile and the Reynolds shear stress profile at some selected locations beneath the block were analyzed. The analysis suggested that the mean velocity, the turbulence intensity and the Reynolds shear stress were greatly enhanced by increasing Froude number and t/h ratio within the recirculation region and started to decrease after the recirculation region. This finding supports the breakup of large scale vortical structures dominating the recirculation region formed beneath the ice block due to the flow separation at the leading edge. The results also demonstrated that the presence of an ice block in a channel could alter the flow field locally from open water conditions.

ACKNOWLEDGMENTS

I would like to thank my supervisor, Dr. Karen Dow for her guidance during this research. I also thank Dr. Shawn Clark and Dr. Mark Tachie for their valuable comments and guidance.

I greatly acknowledge Dr. Baafour Nyantekyi-Kwakye for the countless stimulating discussions during my study.

I would like to acknowledge the financial support from GETS and my supervisor.

I am thankful to Sviatoslaw Karnaoukh, Alex Wall and my lab mates for their help through this research.

Last but not least, my deepest gratitude goes to my parents, sisters, in-laws and in particular my loving husband and my two precious kids for their encouragement and support throughout my life.

DEDICATION

In loving memory of my mother, Fatema Jinnah (1950 - 2019).

TABLE OF CONTENTS

LIST OF FIGURES

LIST OF TABLES

LIST OF VARIABLES

b = width of the ice block

C = integral constant

C_f = skin friction coefficient

d_p = particle diameter

d_{pitch} = pixel pitch

F_r = Froude number of approach flow

g = gravitational acceleration

h = approach flow depth

k = kinetic energy

κ = von Karman constant

L = length of the ice block

L_r = reattachment length

M_f = magnification factor

R_e = Reynolds number of the approach flow

t = thickness of the ice block

t_p = response time

U = mean streamwise velocity

U_c = critical velocity for submergence

U_e = free stream approach velocity

U_m = local streamwise maximum velocity

U^* = normalized streamwise velocity

U_τ = shear velocity

u' = streamwise turbulence intensity

v' = vertical turbulence intensity

$-uv$ = Reynolds shear stress

W_{ia} = interrogation area window size

x = streamwise distance measured from the block's leading edge

y = distance from the channel bed

ρ_f = density of the fluid

ρ_i = density of ice

ρ_p = density of the particle

ρ_w = density of water

μ_f = fluid viscosity

ν = kinematic viscosity

δ = boundary layer thickness

$\delta*$ = displacement thickness

θ = momentum thickness

Π = coles wake parameter

τ_i = boundary shear stress beneath the ice block

τ_b = boundary shear stress at the channel bed

Δt = time delay

Δs = local displacement vector

Chapter 1 : INTRODUCTION

1.1 Motivation

River ice jam has major social, economic and ecological impacts as it can reduce hydropower generation, produce extreme flood events and damage both lives and property in different parts of Canada and other cold regions. Ice jams may occur at the upstream end of a solid or fragmented ice cover, narrow sections, junctions, places where the cross-section of river channel suddenly reduces. In the formation of ice jams, ice blocks play a prominent role, whether at freeze-up or at breakup. The accumulation of ice blocks can restrict the channel flow and can result in ice jams that may produce extensive backwater effects of flooding (Uzuner & Kennedy, 1972). Floating ice blocks can be stopped by a stationary ice cover or they can be entrained by the flow. Once entrained, they can deposit beneath an intact ice cover which potentially could lead to the formation of a thickened ice jam (Beltaos, Carter, & Rowsell, 2012). On the other hand, the entrained ice blocks have the potential to crack and weaken the restraining ice cover, which could lead to an ice jam release event (Jasek, 2003). However little knowledge exists about the actual physics surrounding an individual ice block and the hydrodynamic forces that act on it (Ambtman, 2009). Ice block stability is influenced by the flow separation at its leading edge. Flow separation causes pressure reduction beneath the ice block, which has a potential impact on its stability. It is important to understand the flow dynamics beneath an ice block to understand the mechanics of the development of river ice jams, to design ice booms and ice retention facilities on rivers, to design a channel with a stable ice cover or to understand the upstream progression of ice cover composed of arriving ice blocks. The measurement of the flow beneath an ice block in the field is inherently difficult due to safety concerns and technical issues.

Previous researchers have carried out experimental studies on the stability of ice blocks such as Larsen (1975), Uzuner and Kennedy (1972), Ashton (1974), Daly and Axelson (1990), Coutermarsh and McGilvary (1994), Dow-Ambtman et al. (2011) and Zhao et al. (2017). All of these researchers identified the reason for instability was the pressure reduction beneath the block as a result of flow separation and acceleration. Early researchers focused on the identification of critical conditions at instability, such as densimetric Froude number. More recent work quantified the underturning moment and submerging force at which the floating ice blocks become unstable. Ambtman (2009) first used digital particle image velocimetry (DPIV) and observed flow separation and reattachment beneath floating blocks of different thickness-to-depth ratio and leading-edge shape keeping the Froude number constant. Nyantekyi-kwakye et al. (2017) carried out an experimental investigation of turbulent flow characteristics beneath a simulated ice jam using particle image velocimetry. However, there is still a need to investigate turbulent flow beneath an ice block.

Understanding the flow fields beneath an ice block is a major challenge in the field of river ice engineering. Recently, there has been a growing need to conduct studies that will fully elucidate the flow dynamics beneath an ice block. In previous years, different traditional techniques have been used to measure mean flow under ice cover that are intrusive and time consuming since they produce point wise measurements; for example using various current meters, acoustic Doppler velocimeter and current profiler (Teal et al., 1994; Walker &Wang, 1997). Also, unsteady velocity profiles beneath a simulated floating ice cover were investigated by Healy et al. (2002) using Prandtl tubes and an acoustic Doppler velocimeter. To date and to the best of the author's knowledge the only investigation on the flow field beneath an ice block using particle image velocimetry (PIV) is reported by Ambtman (2009). With the advent of particle image velocimetry (PIV), flow fields beneath a simulated ice block can be obtained without any disturbance due to its non-invasive measurement and it can provide an insight that is beyond the scope of early research.

The present research seeks to provide a better understanding of flow dynamics at the leading edge beneath an ice block for different Froude numbers and *t/h* ratios to answer the following major questions which are the central topic of the research:

1. How does Froude number affect the flow separation and the velocity field at the leading edge of an ice block that has a potential impact on stability?
2. How does ice thickness-to-depth ratio affect the flow separation and the velocity field at the leading edge of an ice block?

1.2 Objectives

The specific objectives of this research are to:

- Quantify the two-dimensional flow field at the leading edge beneath an ice block with varying Froude numbers and ice thickness-to-depth ratios using particle image velocimetry.
- Quantify and analyze the mean velocity, flow separation, turbulence intensity, Reynolds shear stress and boundary shear stress beneath an ice block with varying Froude numbers and ice thickness-to-depth ratios.

1.3 Outline of the thesis

The following section of this thesis, Chapter 2, contains a literature review of ice block stability, flow separation and particle image velocimetry application in the study of flow separation and reattachment. The laboratory set-up, including the flume and apparatus used for the research, and experimental conditions are presented in Chapter 3. Chapter 4 contains a paper describing the detail results of the experimental analysis. Conclusions and recommendations for future work are included in Chapter 5.

Chapter 2 : LITERATURE REVIEW

This chapter will first provide an introduction on flow features beneath an ice block and the dimensional analysis of variables that influence ice block stability. Afterward, in order to better understand the flow characteristics beneath an ice block, a brief introduction of the flow characteristics including velocity distribution and selected turbulence characteristics will be presented in an open channel and ice-covered channels. Lastly, the current literatures related specifically to the ice block stability will be discussed followed by the principles of particle image velocimetry.

2.1 Flow features beneath an ice block

Figure 2-1 shows a schematic diagram of a rectangular ice block, which has come to rest against a floating obstacle in a fully developed flow region in an open channel where free stream approach velocity is U_e and the approach flow depth is h. The length, width and thickness of the ice block are L, b and t respectively. Approach flow separates at the leading edge of the rectangular block and the separated flow re-attaches beneath the block. The streamwise distance from the leading edge of the block to the reattachment point is known as reattachment length (L_r).

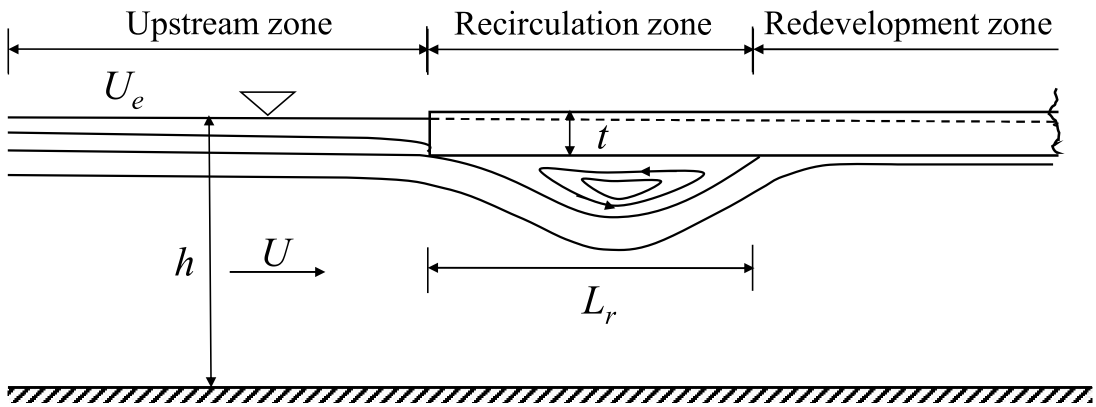

Figure 2-1: Schematic diagram of flow features beneath an ice block

The flow field beneath an ice block can be divided into three distinct regions: an upstream zone, a recirculation zone and a redevelopment zone. The flow characteristics in the upstream zone are similar to those of a fully developed channel flow. The recirculation zone spans from the leading edge of the block to the reattachment point within which the recirculation bubble occurs beneath the ice block just after the flow separation. Beyond the reattachment point, the shear layer redevelops into a new boundary layer, known as the redevelopment zone. The stability of an ice block depends on the flow characteristics at the leading edge as well as leading edge shape. For the present study, the dimensional analysis has been adapted from Ambtman (2009) given in Equation 2-1, which suggests that for solid blocks of rectangular shape, the critical velocity for submergence U_c, is a function of the following variables.

$$U_c = f\ (t, b, L, h, \rho_w, \rho_i, g) \qquad \text{Equation 2-1}$$

Where the density of water is ρ_w, the density of ice is ρ_i and gravitational acceleration is g. The non-dimensional form of these variables can be obtained as follows:

$$\frac{U_c}{\sqrt{gh}} = f\left(\frac{t}{h}, \frac{t}{L}, \frac{L}{b}, \frac{\rho_i}{\rho_w}\right) \qquad \text{Equation 2-2}$$

2.2 Flow characteristics in open channel and channels covered with ice

In open channel flow, the water surface always has contacts with atmospheric pressure. Natural channels like rivers and creeks, as well as in artificial channels such as irrigation canals, flumes and wastewater channels are referred to as open channel flow. Flow in most open channels is turbulent (R_e > 12500). In an open channel, the existence of the free surface and friction along the boundaries causes the variation of velocity across the channel section (Chow, 1959). In open channels, the flow velocity is low near the bed (solid boundaries) and increases gradually towards the free surface from the boundary. In general, the maximum velocity in all types of channels is located at 5 to 25 percent of total flow depth below the free surface (Chow, 1959) due to secondary currents (Nezu & Nakagawa, 1993). The flow field in open channels is divided into two layers: the inner layer and the outer layer. The inner layer corresponds to 15% to 20% of the total flow depth (y/h < 0.15-0.2) and the outer layer is for the remainder of the flow depth (0.15-0.2 ≤ y/h ≤ 1) in which y is the distance from the channel bed and h is the total flow depth (Nezu & Nakagawa, 1993). Keulegan (1938) mentioned that in open channels, the logarithmic law can be considered for velocity distribution over the whole depth of flow. However, in the outer layer, the average velocity distribution has a deviation from the logarithmic law due to the wake (Coles, 1956).

The logarithmic law for smooth open channels is as follow:

$$\frac{U}{U_\tau} = \frac{1}{\kappa} ln \frac{yU_\tau}{\nu} + C \qquad \text{Equation 2-3}$$

U is mean streamwise velocity, U_τ is shear velocity, ν is kinematic viscosity, κ is the von Karman constant = 0.41 and C is the integral constant = 5.0.

The Logarithmic law can be applied to the vertical distribution of streamwise velocity both in the bed and ice affected region in case of channels covered with ice. Lau (1982) indicated that the logarithmic distribution was valid for 60% of the flow depth closest to the ice and bed boundary in each flow region but the remaining 40% of the flow depth in each region, which are close to the location of the maximum velocity, there was a deviation from the logarithmic distribution. Yamaguchi and Hirayama (1990) performed three-year field measurements under various ice cover and bed roughness conditions and showed that the vertical distributions of streamwise velocity in both the bed and ice affected region fit well to the logarithmic law. However, their calculated maximum velocity using the logarithmic law was greater than the measured value.

Turbulence intensities describe the turbulence flow fluctuations that are the root mean square of the difference between instantaneous velocity and time average of the instantaneous velocity (Nezu & Nakagawa, 1993). Turbulence intensities in the open channel have a decreasing trend with increasing normalized flow depth (*y/h*) so that the turbulence intensities have a maximum value near the solid boundary and minimum value near the free surface (Nezu & Nakagawa, 1993). The existence of ice in channels can modify the turbulence intensity distributions in channels covered with ice compared to open channels. In ice-covered channels, the dimensionless turbulence intensities decrease with increasing distance from the channel bed to reach their minimum value and then begin to increase towards the ice cover. Therefore, the maximum local turbulence intensities occur near the boundaries, and minimum local ones happen near the plane of zero shear stress (Parthasarathy & Muste, 1994; Robert & Tran, 2012).

The boundary shear stress in ice-covered channels is divided into the shear at the bed and channel banks, and the shear stress at the underside of an ice cover. The boundary shear stress distribution can be analyzed using the two-layer hypothesis in ice-covered channels (Zufelt & Ettema, 1997; Gerard, 1980). The average boundary shear stress and local shear stress in the ice and bed affected region can be estimated using the same equations as used for open channels.

2.3 Stability analysis of an ice block in a channel

A moving ice block when arrested by an obstacle, may contribute to the upstream progression of an ice cover or become unstable by one of two methods. One method is vertical submergence or 'sinking' where the hydrostatic resisting force is overcome by the submerging force and the block sinks vertically until the flow carries it downstream. Another method is submergence by 'underturning'. In this case, the moment created by the submerging force rotates the blocks completely about its downstream corner. Some researchers have discussed the entrainment of the block in a half-turned position i.e. entrainment occurs before the block's complete rotation. If the submerged ice blocks carried under the ice cover and deposited a short distance downstream from the leading edge of the cover, lead to the ice jamming. Thus, stability analysis of an ice block can facilitate understanding the underlined physics of ice jams formation. Two critical modes of ice block instability are presented below.

2.3.1 Vertical submergence or 'sinking'

The critical force balance for vertical submergence occurs when the top of the block is at the water surface and is subjected to the maximum submerging force and maximum buoyancy force. The submerging force can be calculated by the pressure reduction beneath the block and the resisting force is computed by the net buoyancy of the ice block. When the submerging force exceeds the maximum buoyancy force, the entire block becomes submerged. According to Uzuner and Kenedy (1972), for very long blocks, the mode of instability is vertical submergence or sinking as the extent of pressure reduction beneath the block is not large and the corresponding force is small compared to the total pressure force acting on the block. Thus the block rotates about its downstream corner little if at all then sinks without significant rotations until the no-spill limit (the distance the block has sunk, equals the difference between the zero-velocity freeboard and the surface velocity head) is met, and after that transported downstream. So, the critical velocity for submergence is smaller for short blocks than for long ones (other factors being the same), because the short blocks experience the pressure reduction over their whole length resulting from flow separation around the the block. The critical condition of submergence can be represented in Figure 2-2.

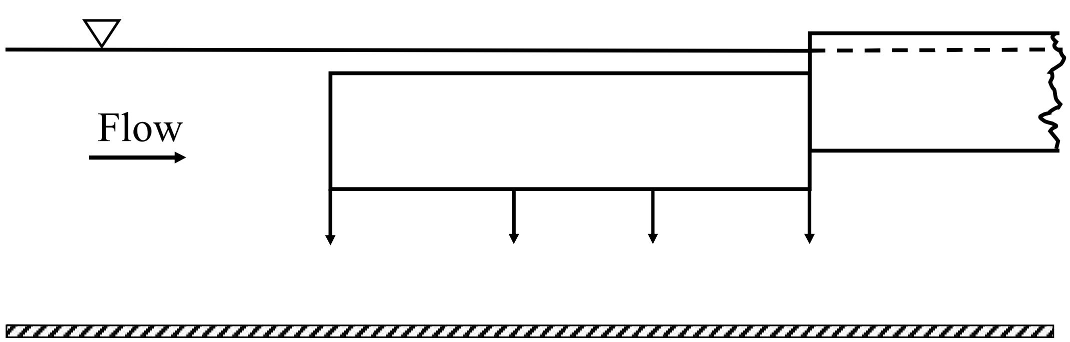

Figure 2-2: Floating ice block beginning sinking (adapted from Ambtman, 2009).

2.3.2 Underturning

Uzuner and Kennedy (1972) used the "no-spill" condition as ice block instability criteria which can be described as the spilling of water onto the surface of the block and the block would be unstable. Daly and Axelson (1990) conducted a detailed analysis to find ice block instability criteria based on the hydrostatic righting moment that resists the block's rotation. Recently Dow-Ambtman et al. (2011) developed equations through a force-moment analysis to identify ice block stability criteria and compared it with pressure distribution beneath the ice block. Figure 2-3 shows the initiation of the underturning instability of a floating ice block.

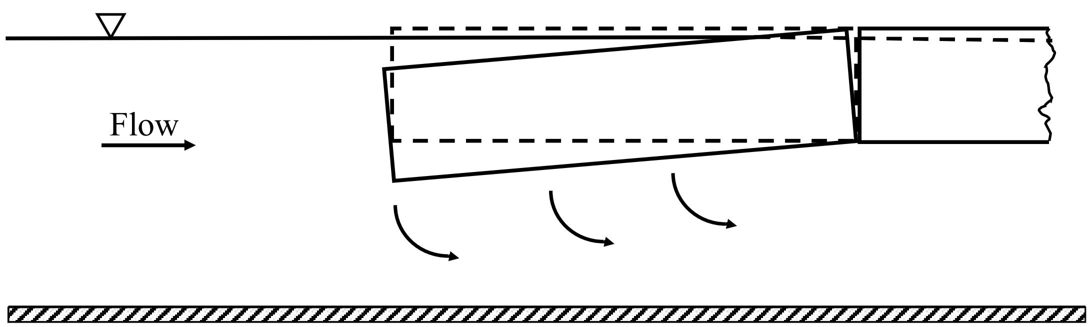

Figure 2-3: Floating ice block beginning underturning (adapted from Ambtman, 2009).

2.4 Basic principles of PIV

The flow is seeded with seeding or tracer particles that follow the flow faithfully. The flow field is illuminated by a double pulsed laser sheet. The scattered light reflected by the seeding particles for the two images is captured using a charged- coupled device (CCD) camera. The two successive images are separated by a time delay, Δt. The image pair is divided into smaller subsections named interrogation areas (IA). To determine the local displacement vector (Δs)

between the first and second images a cross-correlation algorithm is applied to each IA. The velocity vector within each IA is obtained by dividing the Δs by Δt. To obtain the whole velocity vector map the correlation algorithm is repeated for all IA.

The components of the PIV considered to set up the experiment for the present study are provided in the following sections.

2.4.1 Tracer particles

The PIV technique directly measures the velocity of the tracer particles which is considered as the velocity of the fluid. So the tracer particles should be homogeneously distributed within the flow (Westerweel et al. 1996). A rule of thumb is that about ten particles should be present in an IA for correlation. The tracer particles should be large enough to scatter sufficient light to be captured by the camera and should be small enough to faithfully follow the flow. In selecting the appropriate tracer particles, the mean size, specific gravity, shape, width-to-size distribution and refractive index of the particle are some criteria that should be considered. The settling velocity of the tracer particles can be estimated from Stokes law. The settling velocity was determined using Equation 2-4.

$$v_s = \frac{(\rho_p - \rho_f) g\, d_p^2}{18 \mu_f} \qquad \text{Equation 2-4}$$

Where ρ_p and ρ_f are the density of the particle and fluid respectively, g is the acceleration due to gravity, d_p is the particle diameter and μ_f is the fluid viscosity. The tendency of the particles to attain velocity equilibrium within the flow can be measured by the response time, t_p. The response time can be estimated using the formula Equation 2-5 presented in Raffel et al. (1998).

$$t_p = \rho_p \frac{d_p^2}{18\mu_f} \qquad \text{Equation 2-5}$$

2.4.2 Flow illumination source

For most PIV systems, a double-pulsed neodymium-yttrium-aluminum garnet (Nd: YAG) laser is used as a flow illuminating source. The Nd: YAG laser provides monochromatic light with high-intensity illumination to freeze the motion of the flow during imaging. For the illumination of the flow field, a sheet of light is created by the laser-emitted lights after passing through a series of lenses. The length and width of the light sheet can be adjusted according to the field of view.

2.4.3 Data acquisition and Image processing

The CCD camera has scan interline CCD chips which contain both photosensitive cells as well as storage cells. The highly sensitive CCD camera first captures an image on the photosensitive cells, which is transferred to the storage cells and the second image is stored on the photosensitive cells. Both images are then transferred chronologically from the camera to the storage device of the computer. With the high resolution and high frame rates, the camera can maintain an exposure interval Δt of less than 1 μs. The images are sub-divided into small areas called interrogation areas. The average displacement vector is calculated by applying a correlation method on the first and second images on the two frames for each interrogation area. A vector map of the average displacements for all the interrogation areas is produced by either an auto-correlation or cross-correlation method.

2.5 Previous studies

Attention is now turned to the previous studies on the stability of ice blocks and turbulent flow analysis within flow separation and reattachment region. The rationale is to present the background information to understand the relatively more complex phenomena beneath an ice block.

Uzuner and Kennedy (1972) carried out experiments to determine critical Froude number as a function of t/h, t/L and ρ_i/ρ_w , where t is the thickness of the block, L is the length of the block, h is the approach flow depth, ρ_i and ρ_w are the block and water density respectively. They observed that blocks with intermediate length range of $0.1 < t/L < 0.8$, become unstable by underturning while shorter blocks ($t/L > 0.8$) or longer blocks ($t/L < 0.1$) showed the instability by sinking. They identified the reason behind this as for the shorter blocks, the region of separation extends under practically the whole block and for the longer blocks flow acceleration plays a dominant role. They considered the "no-spill" condition as the limit of stability and analyzed the stability through one-dimensional moment analysis and established an empirical moment coefficient.

Ashton (1974) suggested through a dimensional analysis that the densimetric Froude number is the most important parameter to determine the stability criteria of the floating ice block. In addition to this, he found that simple moment analysis showed good agreement with the experimental data of Uzuner and Kennedy (1972). The results also showed that critical velocity for underturning is lower than vertical submergence. However, he suggested replacing the no-spill condition with more formal stability criteria.

Larsen (1975) used paraffin as a simulated ice block in a hydraulic flume to see its stability against a simulated solid ice cover of the plyform sheet which was able to move freely in the vertical direction. Flow velocity was increased by decreasing the depth of flow at a constant discharge to identify the critical velocity of ice floe instability. He observed different modes of submergence and concluded that the local flow properties (velocity and depth of flow) dominate the ice block stability. He also observed that instability occurs when the upstream end of the floe submerged and the critical Froude number for thinner floe was higher.

Daly and Axelson (1990) theoretically analyzed the rotational stability of floating and submerged blocks and developed a general expression for the moment coefficient to find the stability limit of flow conditions. They used previous researchers' data to analyze the limit of stability in terms of densimetric Froude number based on block thickness. They identified the limit of stability both for submerged and floating blocks as the point of rotation at which maximum hydrostatic righting moment is equal to the underturning moment. However, their analysis showed a simple exponential relation of moment coefficient with non-dimensional block thickness along with two parameters depending on the block geometry.

Coutermarsh and McGilvary (1994) measured pressure below the ice block to analyze stability. They found symmetrical pressure distribution along the width of the block and determined the difference between dynamic fluid pressure and static pressure along its entire length. They carried out their experiment for different flow depths, angles of attack and velocities with constant block thickness. They found lower pressure at the leading edge for all cases and underturning moment increases with higher velocity. They defined a coefficient of moment relating the flow depth and flow velocity for a fixed block geometry.

Jasek (2003) observed the initiation of a lead at the downstream of the toe of an ice jam by the sliding ice blocks underneath the ice sheet. He assessed qualitatively based on surface observations on what is going on underneath the ice jam. The study speculated that large ice blocks are carried underneath the ice jam toe by high-velocity currents and released into a somewhat slower and less turbulent flow downstream of an ice jam. These large blocks accelerate vertically upwards due to buoyancy and may impact the solid ice surface, possibly cracking and weakening the cover. These study also signifies that the large ice blocks may have sufficient buoyancy to induce bending moments in the solid ice sheet causing further weakening.

Dow-Ambtman et al. (2011) investigated pressure distribution beneath a simulated floating ice block in a recirculating flume to explore and extend the work of Coutermarsh and McGilvary (1994). In this study, Plexiglas acrylic was used as simulated ice and twenty pressure taps were fitted underside it. The pressure distribution showed an initial decrease to a minimum at the leading edge which sustained some distances from the leading edge and then increase gradually until some distance while being constant for the remaining length of the block. They also observed symmetrical pressure distribution about block's centerline and both higher flow rates and greater thickness decrease pressure below the ice cover while increase initial pressure drop region, submerging force and underturning moment.

Dow-Ambtman et al. (2011) analyzed the stability of floating ice blocks through a force-moment analysis based on dynamic pressure measurement beneath the block with both flat and tilting condition at about 0.3° rotation angle under various thickness-to-depth ratios and flow velocities. The dynamic pressure showed similar initial plateau for both flat and tilting conditions whereas the second pressure plateau was higher for tilting cases than the flat case. The results also showed that the submerging forces, underturning moments and recovery length for Venturi pressure are greater in tilting case than the flat case which signifies less stability associated with tilting case. They calculated critical densimetric Froude number and compared with earlier research (Uzuner & Kennedy 1972; Ashton 1974; Larsen 1975; Daly & Axelson 1990). However, they also found instability due to vertical submergence occurred with higher critical velocity than underturning.

Wang, Wu and Sui (2018) studied the stabilities of ice blocks in front of an ice cover. They carried out laboratory experiments using ice blocks with different dimensions and analyzed forces acting on the ice blocks in front of the ice cover. They observed that the ice blocks can not be entrained if the flow velocity is low enough or the ice block is large enough. They used an equilibrium method to study the stability of an individual ice block at the edge of the ice cover. They found the entrainment process of ice blocks in front of the ice cover depends on two criteria; the dimension of the ice block and the flow velocity. The results also showed that when the ice block is neither so thick nor so thin, Ashton's formula could be used to determine the critical flow velocity for the entrainment of ice blocks, with reasonable results. The study summarized that critical flow velocity for the entrainment of ice blocks not only depends on *t/h* but also on *t/L* and the critical flow velocity for the entrainment of ice blocks decreases with the increase of *t/h*.

Ambtman (2009) first applied particle image velocimetry to investigate flow fields beneath a floating ice block. This study observed that the flow separation and reattachment beneath floating ice blocks for two *t/h* ratios (0.05 and 0.10) with constant Froude number and determined that the minimum pressure location coincided with the peak maximum velocity location for both the *t/h* ratios. This result suggested that the localized flow behavior causes the initial pressure reduction at the leading edge. Also, the length of the separation zone for the rectangular block cases showed good consistency with the position of mid pressure (the streamwise location at which the pressure is midway between the initial and final pressure plateau values). The results showed that the separation and recirculation zone was greater with a higher thickness of the block. Also, the Reynolds stress was higher for a thicker block. The results of this investigation showed good agreement with previous dynamic pressure distribution. Thinner block and thicker block showed different velocity and pressure distribution. Moreover, a localized flow pattern was found responsible for pressure distribution at the leading edge and stabilization occurred at the mean velocity beneath the block.

The flow separation beneath an ice block has similarities to the flow separation that occurs above a forward facing step. This area of research has been more extensively studied using particle image velocimetry. Sherry et al. (2010) carried out an experimental study of the recirculation zone created by a forward-facing step attached to the bottom of a channel within the turbulent boundary layer. In this study, they used particle image velocimetry over a wide range of Reynolds numbers from 1400 to 19000, calculated based on the free stream velocity and the step height. The results showed a linear trend of increasing reattachment length with Reynolds number up to 8500, while the reattachment length was less sensitive to Reynolds number above 8500.

Essel and Tachie (2017) conducted experiments to investigate the effects of Reynolds number on the turbulence structure in the recirculation region of a forward-facing step (FFS). Detailed PIV measurements were performed over a smooth upstream wall and a FFS for three different Reynolds numbers 4940, 8400 and 8650 (based on free stream velocity and step height). The results showed that the relative boundary layer, displacement, and momentum thicknesses do not vary significantly for the range of Reynolds number examined. The flow accelerates past the step and attains a maximum value of 1.3 U_e close to the leading edge of the step, where U_e is the free stream velocity. The reattachment length also increased with the increase in Reynolds number. The Reynolds shear stress topology revealed a region of negative Reynolds shear stress close to the leading edge of the step while Reynolds shear stress is positive on top of the step.

Chapter 3 : EXPERIMENTAL SETUP AND MEASUREMENT PROCEDURE

This chapter presents a detailed description of the experimental setup including test facility, test conditions, the particle image velocimetry (PIV) system. The measurement procedure and measurement uncertainty are also provided in this chapter.

3.1 Test setup

The experiments were conducted in a recirculating open water channel system which was designed and manufactured by Engineering Laboratory Design, Inc., Minnesota, USA. The experimental setup and a schematic diagram of the test section are provided in Figure 3-1 and Figure 3-2 respectively. The length of the main recirculating channel is 2500 mm and the cross-section is 200 × 200 mm^2. The bottom and sidewalls of the water channel were made of Super Abrasion Resistant ® (SAR) clear acrylic plate to facilitate optical access. The main water channel consists of a flow conditioning unit, centrifugal pump, variable speed drive, piping and valves, supporting framework and a filtering system. To condition the flow before entering the water channel, a series of perforated steel plates and honeycombs are fitted within the settling chamber at the inlet section of the water channel. The recirculating flow is driven by a centrifugal pump having a 24 HP variable speed drive motor.

A 50 mm long 24-grit sandpaper glued onto a 4 mm thick acrylic sheet was used to facilitate the rapid development of the boundary layer. This 4 mm thick acrylic sheet, which spans the entire width and length of the water channel, was placed at the entrance of the water tunnel onto the bottom wall of the channel using double-sided tape. Finally, this artificial floor was tightly screwed at both ends onto the bottom of the channel so that it would not lift up during the experiments. A rectangular acrylic block of 500 mm length and 25 mm thickness spanning the entire width of the channel was suspended from the top of the channel with the help of threaded rods, an aluminum plate and clamps as shown in Figure 3-3. The block was positioned vertically by adjusting the threaded rods to the desired elevation and using a level to ensure the block was level. The water depth and block height were measured using a measuring scale. Various thicknesses of the floating ice block were created by moving the block up or down using four threaded rods assuming a specific gravity of ice of 0.92. The block was positioned in the flume at 1500 mm from the entrance of the test channel. This position was chosen by examining the flow development in the flume through particle image velocimetry measurement in open water conditions for the same range of Froude numbers. The x coordinate represented the streamwise flow direction; y coordinate showed the vertical flow direction and z coordinate defined the transverse flow direction.

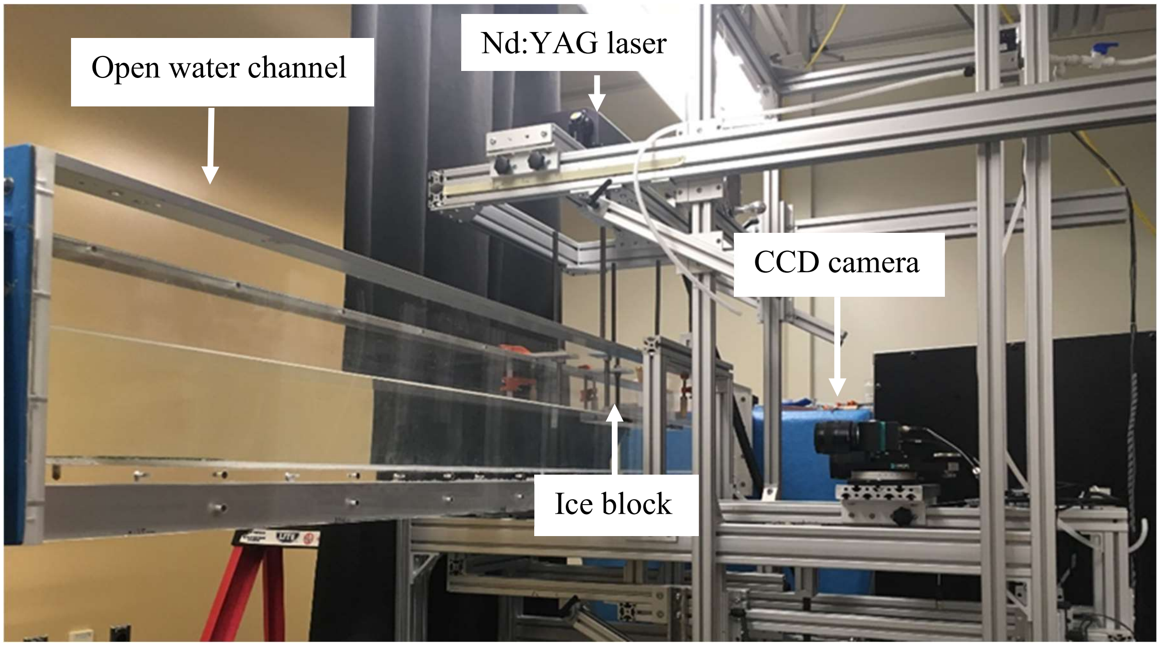

Figure 3-1: Picture of recirculation open channel and components of the PIV system.

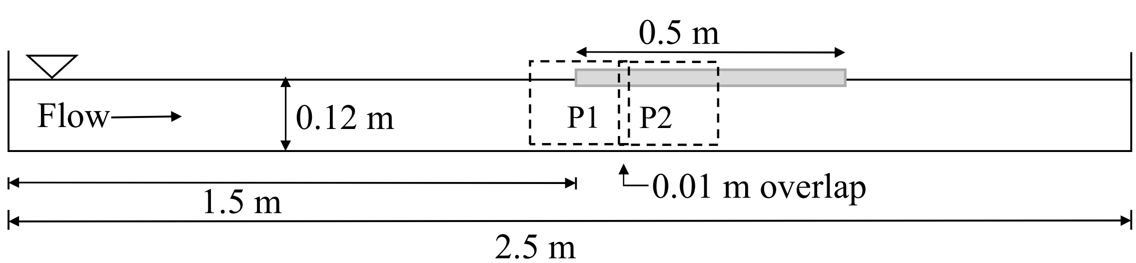

Figure 3-2: Schematic diagram of the experimental setup with rectangular acrylic blocks.

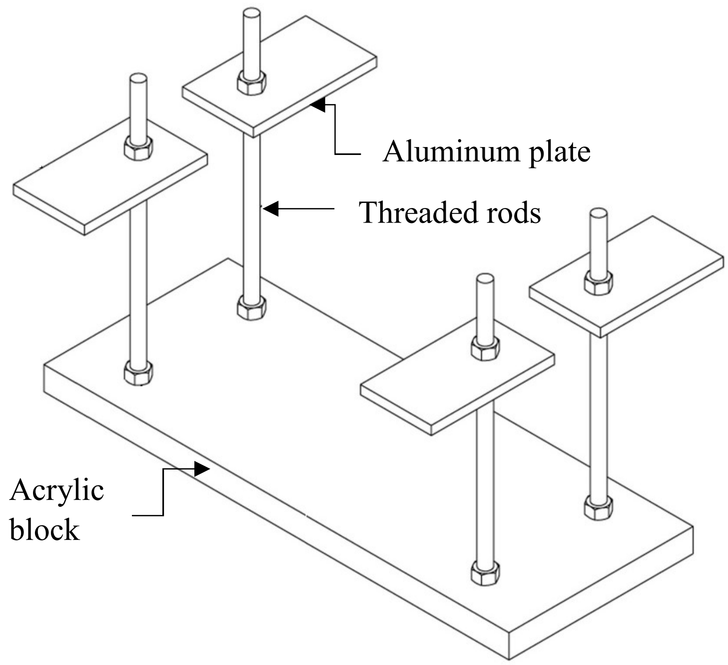

Figure 3-3: Schematic diagram of the rectangular acrylic blocks with threaded rods, aluminum plate and clamps.

3.2 Test conditions

The detailed test conditions presented below in Table 3-1. For open water condition analysis four Froude numbers were used, with constant flow depth. To enable the simulation of various Froude numbers, the frequency of the pump was changed to achieve the specific flow velocity. Uzuner and Kennedy (1972) stated that typically the initial Froude number will be in the range of 0.20 to 0.50 in a river with stationary ice at some location along its length. Based on the present experimental facility, trial runs and first PIV study on ice by Ambtman (2009), four Froude numbers 0.20, 0.28, 0.34, 0.40 were selected to conduct the experiments for both open water condition and with the presence of ice block. To enable the simulation of *t/h* ratio, the approach flow depth, *h*, was held approximately constant at 0.12 m for the tests with three different ice thicknesses of 0.012 m, 0.018 m and 0.021 m. The *t/h* ratio tests were completed with a constant Froude number of 0.28.

Table 3-1: Test conditions.

Channel without ice block (open water condition)				
Run #	***U (m/s)***	***h (m)***	F_r	R_e
1	0.22	0.12	0.20	26400
2	0.31	0.12	0.28	37680
3	0.37	0.12	0.34	44520
4	0.44	0.12	0.40	52800
Channel with ice block				
Run #	***t (m)***	***h (m)***	***t/h***	F_r
5	0.012	0.12	0.10	0.20
6	0.012	0.12	0.10	0.28
7	0.012	0.12	0.10	0.34
8	0.012	0.12	0.10	0.40
9	0.018	0.12	0.15	0.28
10	0.021	0.12	0.18	0.28

3.3 PIV system

The velocity measurements were performed using a particle image velocimetry (PIV) system which is a whole field non-intrusive velocity measurement technique that measures instantaneous velocity vectors within the flow field. The laser source illuminates the flow field, while the camera captures images of the flow field and the data acquisition system is required to acquire and process the captured images.

In the present study, silver-coated hollow glass spheres have been used as the seeding particle. The mean diameter and specific gravity of the seeding particle are 10 µm and 1.4 respectively. The settling velocity and response time of the seeding particles were estimated as 1.56×10^{-5} m/s and 7.78×10^{-6} s, respectively (Nyantekyi-Kwakye, 2016). This settling velocity is negligibly small compared with the approach velocity and the particle response time is negligibly small in comparison with the time scale associated with flow structure in the present study. Based on these analyses, it was concluded that the seeding particles can follow the flow faithfully. A New Wave Solo Nd: YAG double pulsed laser system has been used to illuminate the flow field. The maximum energy of the laser system was 120 mJ/pulse at 532 nm wavelength.

The thickness of the laser sheet was approximately 1 mm within the field of view of the camera, which coincided with the centerline of the channel to take the measurement in the x-y plane with minimum background noise. Scattered light from the tracer particles was captured with a 12-bit FlowSense EO 4M CCD camera, mounted perpendicular to the *x–y* plane, that has a resolution of 2048 pixels × 2048 pixels and a pixel pitch of 7.4 µm. The CCD camera was fitted with a green bandpass filter of wavelength 530 nm. The time interval (Δt) between pulses was selected such that the particles do not leave the interrogation area entirely (Zhang, et al., 2018). For this reason, an appropriate time interval between pulses was estimated such that maximum particle displacement smaller than 25% of the interrogation area size which will allow the particles to move a detectable amount. Equation 3-1 can be used to estimate the time interval between pulses.

$$\Delta t = \frac{W_{IA} \times d_{pitch}}{4 \times M_f \times U_m} \qquad \text{Equation 3-1}$$

where W_{IA} is the interrogation area window size, d_{pitch} is the pixel pitch, M_f is the magnification factor and U_m is the maximum velocity of the flow.

Measurements were performed in two different x-y planes as shown in Figure 3-2 with a 10 mm overlap, where the first plane captured the leading-edge of the ice block. The field of view for each of these planes was set to 133 mm × 133 mm. An interrogation area (IA) size of 32 pixels × 32 pixels with a 50% overlap was employed to process the instantaneous velocity data resulting in a vector spacing of 1.04 mm × 1.04 mm. A convergence test was conducted to determine the appropriate number of instantaneous images required for this study. From the results obtained by analyzing the mean flow field and turbulent statistics using different sample sizes (1000, 2000, 3000, 4000, 5000, 6000, 7000, 8000, 9000 and 10000 images), 8000 instantaneous images were determined to be sufficient to compute the mean velocities and turbulence statistics. In each test, a trial run with fewer images has been performed before the final run to check the adequacy of the presence of tracer particles. Figure 3-4 represents the convergence test of these quantities.

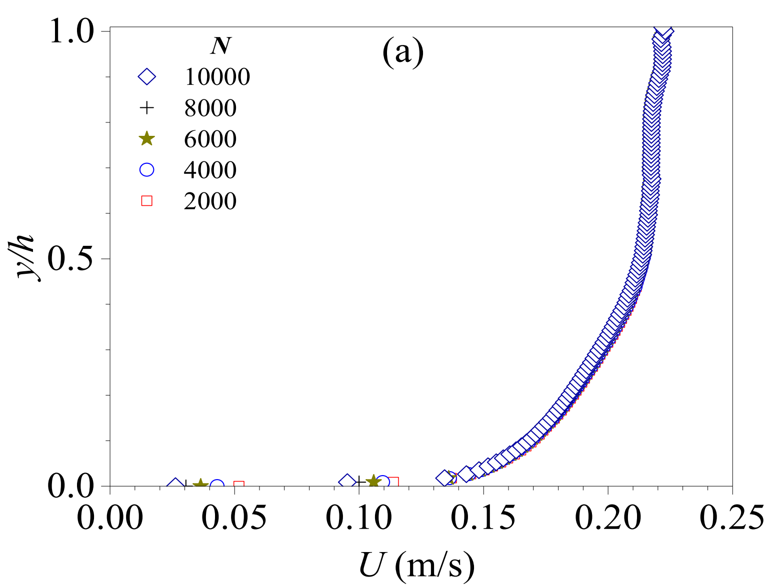

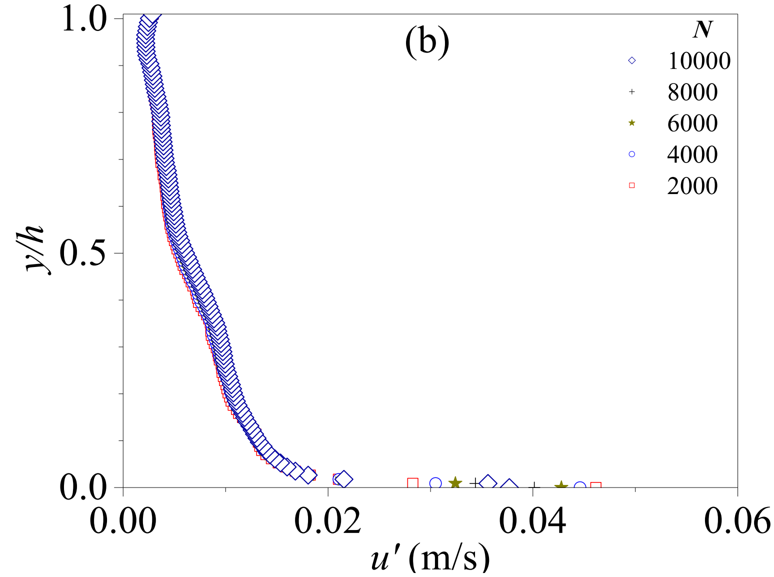
(b)
N
10000
8000
6000
4000
2000
y/h
1.0
0.5
0.0
0.00
0.02
0.04
0.06
u′ (m/s)

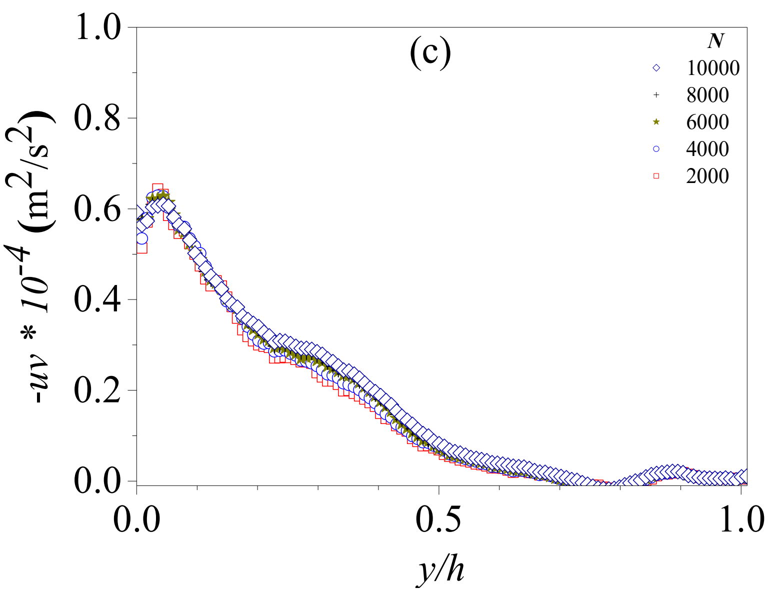
(c)
N
10000
8000
6000
4000
2000
-uv * 10^-4 (m^2/s^2)
1.0
0.8
0.6
0.4
0.2
0.0
0.0
0.5
1.0
y/h

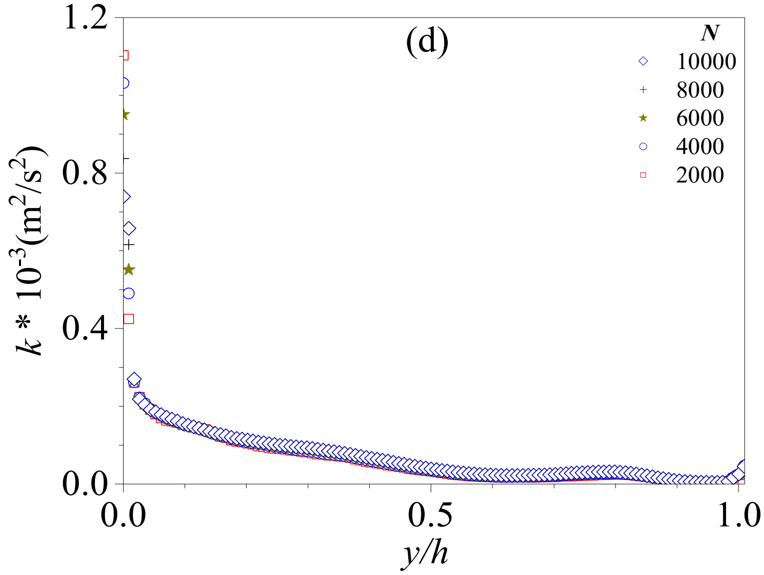

Figure 3-4: Convergence test a) mean velocity b) turbulent intensity c) Reynolds shear stress d) kinetic energy.

The post-processing of the instantaneous images was accomplished by the adaptive correlation option of DynamicStudio developed by Dantec Dynamics. The adaptive correlation utilizes a multi-pass fast Fourier transform cross-correlation algorithm to determine the average displacement of the particles within the interrogation area. The particle displacement was determined using a three-point Gaussian curve fit. An in-house MATLAB code was used to calculate the mean velocities and higher-order turbulence statistics for both planes. The MATLAB code created a set of Excel files containing profiles of each of these statistics which were analyzed by Origin 2017. Contour plots were prepared from the data file created by the MATLAB code using the Tecplot 360 software.

3.4 Measurement uncertainty

A measurement uncertainty analysis was undertaken following the American Institute of Aeronautics and Astronautics (AIAA) standard described by Coleman & Steele (1995) and procedures described in Prasad et al. (1992) and Forliti et al. (2000). The measurement uncertainty for the PIV experiments was calculated by considering the bias, precision and sampling errors. The PIV system was carefully set up to minimize the measurement errors introduced by seeding particles, sub-pixel displacement bias, particle response to fluid motion, laser sheet positioning, etc. A large number of samples (8000) reduces the precision errors for the mean velocities compared to the corresponding bias error. The uncertainty of the mean velocities at 95% confidence level was 0.4% of streamwise mean velocity and 0.2% of vertical mean velocity. The uncertainties in the turbulence intensities and Reynold shear stress are 1.5% and 2.2% of the peak values, respectively. Complete uncertainty analyses have been provided in Appendix A.

Chapter 4 : **PARTICLE IMAGE VELOCIMETRY STUDY OF TURBULENT FLOW BENEATH AN ICE BLOCK**

*This is a draft of a paper that will be submitted to the Journal of Hydraulic Engineering or the Journal of Hydraulic Research co-authored by Karen Dow, Baafour Nyantekyi-Kwakye.

4.1 Introduction

Transported ice blocks in a river can be stopped by a stationary ice cover resulting in the upstream progression or become entrained potentially leading to ice jam formation. The stability analysis of these blocks can give insight into the development of river ice jams or the upstream progression of ice cover. The flow dynamics beneath a floating ice block can help to understand the conditions that affect ice block stability. Detailed velocity measurement can help to analyze the turbulent flow fields beneath an ice block. However, the detailed velocity measurement beneath an ice block in the field is inherently difficult due to safety concerns and technical issues. Thus understanding the flow field at the leading edge beneath an ice block remains as one of the major challenges in river ice engineering.

Previous researchers have carried out experimental studies on the stability of ice blocks. Larsen (1975) observed different modes of instability and concluded that the incipient instability depends on local properties of the flow such as velocity and depth of flow. The densimetric Froude number was reported as stability criteria of floating ice block by Ashton (1974) and found that a higher thickness of ice-to-depth of flow ratios (*t/h*) reduces the critical densimetric Froude number for entrainment. Daly and Axelson (1990) theoretically analyzed the rotational stability of floating blocks in terms of the densimetric Froude number and was found to match the trend of experimentally measured densimetric Froude numbers of Uzuner and Kennedy (1972), Larsen (1975) and Ashton (1974). Coutermarsh and McGilvary (1994) and Dow-Ambtman et al. (2011) measured pressure beneath the ice block to analyze the stability. They observed a symmetrical pressure distribution about the block's centerline and an increased pressure drop region at the leading edge of the block. They also obtained high value of submerging force and underturning moment for both higher Froude numbers and greater *t/h* ratio of the ice block. All of these researchers identified the reason for instability was the pressure reduction beneath the block as a result of flow separation and acceleration. Ambtman (2009) first used digital particle image velocimetry (DPIV) and observed flow separation and reattachment beneath floating ice blocks for two *t/h* ratios (0.05 and 0.10) with constant Froude number and determined that the minimum pressure location coincided with the peak maximum velocity location for both the *t/h* ratios. This result suggested that the localized flow behavior causes the initial pressure reduction at the leading edge. Also, the length of the separation zone for the rectangular block cases showed good consistency with the position of mid pressure (the streamwise location at which the pressure is midway between the initial and final pressure plateau values). Thus, the flow separation beneath the ice block and profiles of the mean velocities and turbulent quantities in the recirculation and reattachment regions may play an important role in the analysis of ice block stability.

Since ice block stability can be linked to the flow, advanced flow visualization techniques and numerical studies can be adopted to quantify relevant flow characteristics to elucidate varying stability criteria for ice blocks. With the advent of particle image velocimetry (PIV), flow fields beneath a simulated ice block can be obtained and can provide insight, which was beyond the scope of early research. To fully elucidate the flow dynamics beneath an ice block, the objectives of the present study were selected to quantify the velocity fields in response to different Froude numbers and *t/h* ratios at the leading edge beneath an ice block. To fulfill this objective, experiments were carried out using PIV, as this will provide better flow visualization in safe, controlled laboratory settings.

4.2 Experimental setup and procedure

The experiments were conducted in a recirculating open water channel system made from transparent acrylic to facilitate optical access. The experimental setup and schematic diagram of the experimental channel are provided below in Figure 4-1 and Figure 4-2 respectively. The length of the channel is 2.5 m and has a square cross-section of 0.2×0.2 m^2. A 24-grit sandpaper (0.05 m long and spanning the entire width of the channel) was used to trip the flow to facilitate the rapid development of the turbulent boundary layer. The open water depth, h, was maintained at 0.12 m. In open water conditions, velocity measurements were conducted in a fully developed region to characterize the open channel flow and boundary layer development. The ice block was constructed from 0.025 m thick acrylic with a length of 0.5 m and spanned the entire channel width of 0.2 m. The block was positioned in the flume 1.5 m from the entrance of the test channel where the flow was known to be fully developed. The block was suspended from the top of the channel with threaded rods. Various *t/h* ratios were conducted by moving the block up or down using four threaded rods. The Cartesian coordinate system is adopted with the x-coordinate aligned with the streamwise direction and the y-coordinate is aligned with the vertical direction; $x = 0$ is at the leading edge of the block and $y = 0$ is on the bottom of the field of view. The streamwise and vertical mean velocities are denoted, respectively, by U and V while root-mean-square values of the corresponding fluctuations are denoted by u' and v' respectively. The detailed test conditions are presented in Table 4-1.

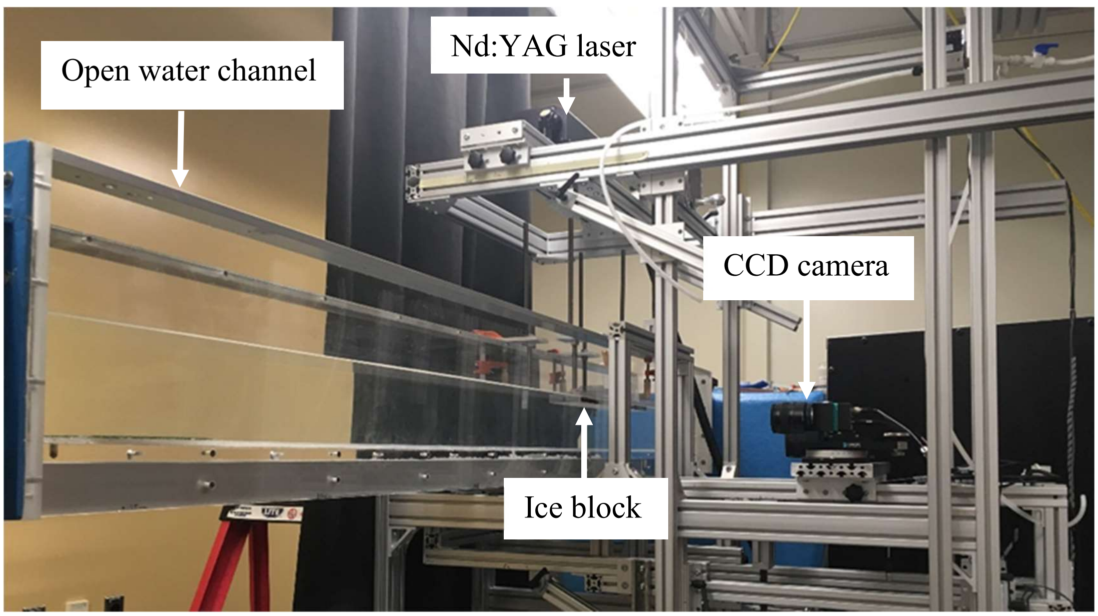

Figure 4-1: Experimental setup.

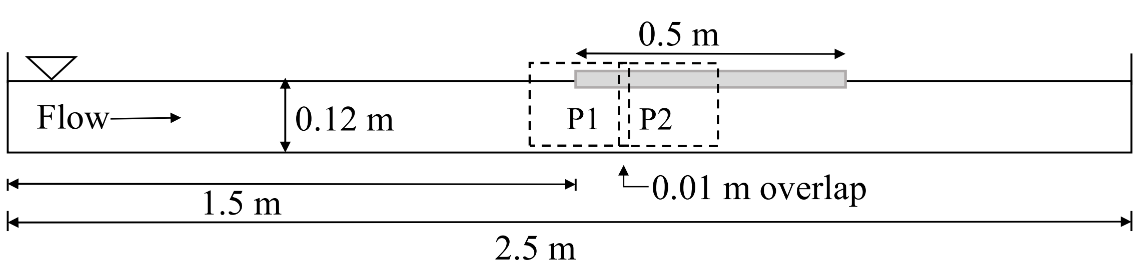

Figure 4-2: Schematic diagram of the experimental setup with rectangular ice blocks.

Table 4-1. Test conditions.

Channel without ice block (open water condition)				
Run #	***U (m/s)***	***h (m)***	F_r	R_e
1	0.22	0.12	0.20	26400
2	0.31	0.12	0.28	37680
3	0.37	0.12	0.34	44520
4	0.44	0.12	0.40	52800
Channel with ice block				
Run #	***t (m)***	***h (m)***	***t/h***	F_r
5	0.012	0.12	0.10	0.20
6	0.012	0.12	0.10	0.28
7	0.012	0.12	0.10	0.34
8	0.012	0.12	0.10	0.40
9	0.018	0.12	0.15	0.28
10	0.021	0.12	0.18	0.28

A planar particle image velocimetry system was used to conduct detailed velocity measurements. Silver coated hollow glass spheres of 10 μm with a specific gravity of 1.4 were used as the seeding particle. A New Wave Solo Nd:YAG double pulsed laser system was used to illuminate the mid-span of the channel. The thickness of the green light sheet was 1.0 mm to reduce the number of de-focused particles. The maximum energy of the laser system was 120 mJ/pulse at 532 nm wavelength. To ensure a reduction in lost correlation, the time interval between the laser pulses was chosen such that the maximum particle displacement was smaller than 25% of the interrogation area size. Scattered light from the tracer particles was captured with a 12-bit FlowSense EO 4M CCD camera, mounted perpendicular to the *x–y* plane, that has a resolution of 2048 pixels × 2048 pixels and a pixel pitch of 7.4 μm. The f-number of the lens was 5.6.

In open water conditions, measurements were taken in the fully developed flow region at x = 1.5 m for various Froude numbers as presented in Figure 4-2. Measurements beneath the ice block were performed in two different x-y planes as shown in Figure 4-2 with a 10 mm overlap, where the first plane captured sections of the open water and the leading-edge of the ice cover. A camera field of view of 133 mm ×133 mm was used. An interrogation area (IA) size of 32 pixels × 32 pixels with a 50% overlap in the streamwise (x) and vertical (y) directions were employed to process the instantaneous velocity data resulting in a vector spacing of 1.04 mm × 1.04 mm. Based on a convergence test, the mean velocities and turbulence statistics were calculated using 8000 instantaneous image pairs captured at a rate of 4 Hz. The post-processing of the instantaneous images was accomplished by the adaptive correlation option of Dynamic Studio developed by Dantec Dynamics. An in-house MATLAB code was used to calculate the mean velocities and higher-order turbulence statistics. Reflection at the free surface and at the channel bed affected the quality of the images and therefore data processing; those data points were removed post processing. The uncertainty of the mean velocities at 95% confidence level was 0.4% of streamwise mean velocity and 0.2% of vertical mean velocity. The uncertainties in the turbulence intensities and Reynolds shear stress are 1.5% and 2.2% of the peak values, respectively following the American Institute of Aeronautics and Astronautics (AIAA) standard described by Coleman and Steele (1995), Prasad, Adrian, Landreth and Offutt (1992), Forliti, Strykowski and Debatin (2000) and Casarsa and Giannattasio (2008).

4.3 Results and discussion

The results will be presented in twofold. The first part will critically investigate the Froude number variation in open water conditions. The second part will discuss the effect of various Froude numbers and thickness-to-depth ratios on the flow dynamics beneath an ice block.

4.3.1 Flow in open water condition

4.3.1.1 Upstream boundary layer parameter

The boundary layer parameters were calculated for different Froude numbers in open water condition. The pertinent boundary layer parameters for the approach flow are summarized in Table 4-2. U_e is the freestream velocity, δ is the boundary layer thickness defined as the vertical distance from the channel bed where the local mean velocity equals 99% of the freestream velocity. δ^* is the displacement thickness was estimated from Equation 4-1 below; indicates the distance the wall has to be displaced to maintain the same mass flow rate as for a non-viscous flow, θ is the momentum thickness, was estimated from Equation 4-2, C_f is the skin friction coefficient was estimated from Equation 4-3 and Π is the Coles wake parameter. The Clauser technique was adopted to estimate the friction velocity, U_τ. In the wall region, y/h < 0.2, Coles wake parameter can be neglected and in the outer region, Coles wake parameter describes the deviation from the log-law (Nezu & Nakagawa, 1993).

$$\delta^* = \int_0^\delta \left(1 - \frac{U}{U_\delta}\right) dy \quad \text{Equation 4-1}$$

$$\theta = \int_0^\delta \frac{U}{U_\delta}\left(1 - \frac{U}{U_\delta}\right) dy \quad \text{Equation 4-2}$$

$$C_f = 2\left(\frac{U_\tau}{U_e}\right)^2$$ Equation 4-3

Both the displacement and momentum thicknesses increased with the increasing Froude number as expected (Singh, 2013). Coles wake parameter (*Π*) increases with the increase in Froude number which can be attributed to the reduction of the free surface effects with the increase in freestream velocity. Rona and Grottadaurea (2010) describes a positive correlation between Coles wake parameter (*Π*) and Reynolds number (calculated from upstream mean velocity and flow depth). Skin friction coefficient, C_f, indicates the drag imposed on the flow by the smooth surface was found to decrease with the increase in Froude number as in the early study by Parthasarathy and Muste (1994). According to Nezu and Nakagawa (1993)), as Coles parameter increases, the skin friction coefficient decreases. This was observed in the present experimental conditions as the value of C_f decreases with increasing of *Π* parameter.

Table 4-2. Boundary layer parameters in open water conditions.

F_r	U_e (m/s)	δ (mm)	δ* (mm)	θ (mm)	U_τ (m/s)	C_f	Π
0.20	0.22	107.42	9.21	7.41	0.0099	0.0040	0.10
0.28	0.32	107.20	11.59	9.16	0.0130	0.0034	0.23
0.34	0.38	106.63	12.91	9.87	0.0145	0.0030	0.49
0.40	0.44	105.47	13.93	10.58	0.0165	0.0028	0.54

4.3.1.2 Profiles of mean velocity, turbulence intensity and Reynolds shear stress

The logarithmic law profile of the streamwise mean velocity over the smooth wall is shown in Figure 4-3 (a). The streamwise mean velocity, *U* and vertical distance, *y* were normalized by U_τ

and ν/U_τ (where ν is kinematic viscosity). The continuous black line represents the classical smooth wall log law (Equation 4-4; where, κ = 0.41 and C = 5.0 (Shah & Tachie, 2008)). For all Froude numbers, the log region started from $y^+ > 30$ and agrees with the classical log law in the overlap region ($30 < y^+ < 250$). The length of the log region decreases with the increase in the Froude number. This might be due to the increase in the Froude number causes an increase in Π values.

$$U^+ = \frac{1}{\kappa}\ln y^+ + C \qquad \text{Equation 4-4}$$

Figure 4-3 (b) shows the normalized streamwise mean velocity (U) in the outer coordinates. Turbulence intensity (u') and Reynolds shear stress ($-\overline{uv}$) are shown in Figure 4-3 (c) and Figure 4-3 (d) respectively. The velocity and length were normalized by the free stream velocity (U_e) and boundary layer thickness (δ) of the respective Froude number to represent mean velocity (U) in the outer coordinates, turbulence intensity (u') and Reynolds shear stress ($-\overline{uv}$) profiles. It can be seen from Figure 4-3 (a) that the normalized streamwise velocity increases from the bed towards the free surface but the maximum velocity occurred beneath the free surface due to the dip phenomenon. The dip in the freestream velocity is because of secondary flows that dominate the free surface. The profile of turbulence intensity and Reynolds shear stress from the bed to the free surface in open water conditions were found similar to the profile observed by Nezu and Nakagawa (1993) as both turbulence intensity and Reynolds shear stress higher near the bottom. For both turbulence intensity (u') and Reynolds shear stress ($-\overline{uv}$) profiles the peak value for different Froude numbers occurred close to bed while decreased farther away from the bed within the outer region of the flow.

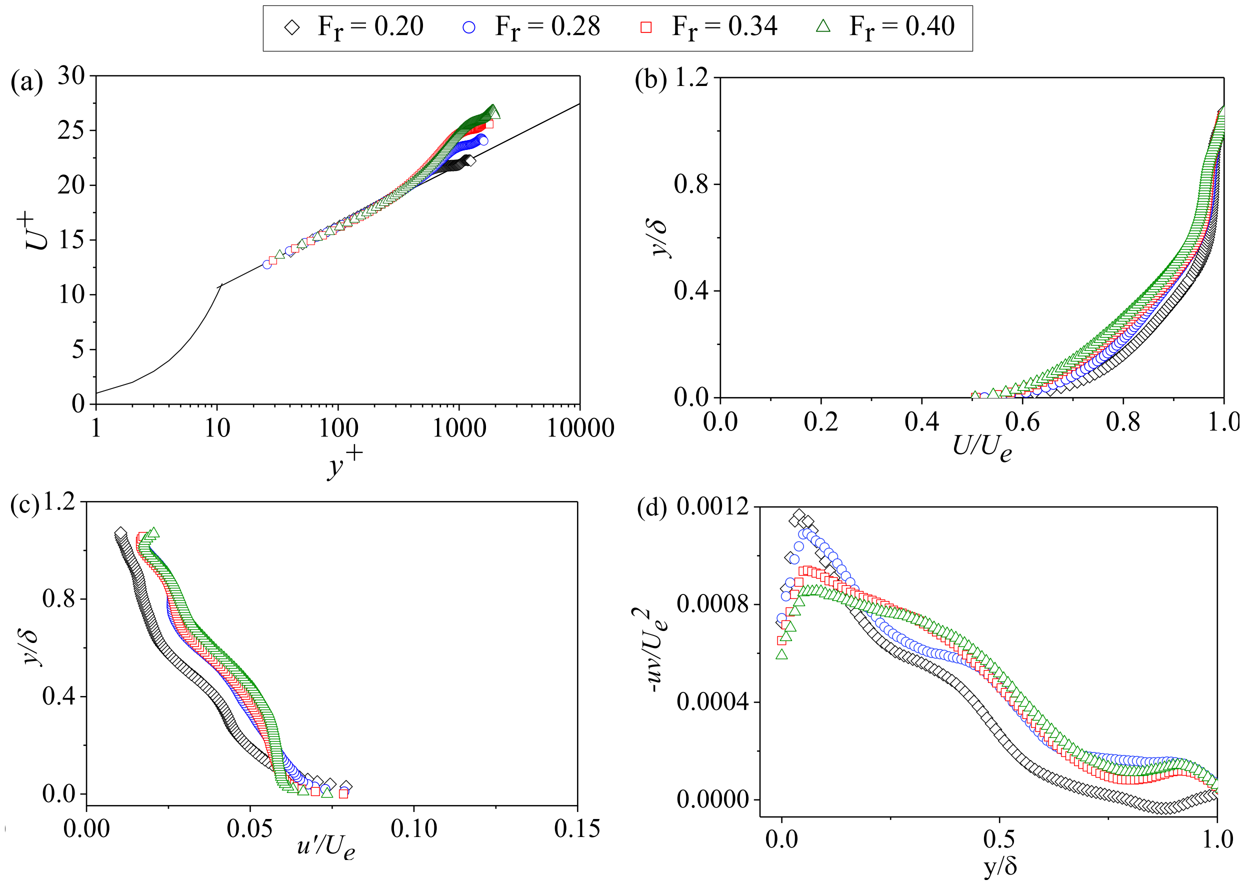

Figure 4-3: Profiles in open water condition (a) streamwise velocity in inner coordinates (b) streamwise velocity in outer coordinates (c) streamwise turbulence intensity (d) Reynolds shear stress.

4.3.2 Flow beneath an ice block

4.3.2.1 Contours of Mean velocity

Figure 4-4 shows the contours of normalized streamwise mean velocities for different Froude numbers and thickness-to-depth (t/h) ratios at the leading edge of the ice block where x = 0 is at the leading edge of the block and y = 0 is on the bottom of the field of view. U_e and h were selected as the velocity and length scales, respectively. Generally, the approach flow separated at the leading edge of the block forming a recirculation zone and subsequently reattaching beneath the block. The reattachment length, L_r, is defined as the distance between the upstream edge of the block and the reattachment point beneath the block. The reattachment length increased with the increase in Froude number and *t/h* ratios as can be observed from Figure 4-4 (using the zero contour line in the streamwise velocity contour plots). From the contours, it can be seen that for all the Froude numbers with constant *t/h* ratio (0.10) the normalized velocities adjacent to the leading edge of the ice block increased by 20% (i.e. $U^* = U/U_e = 1.2$) compared to the respective free stream velocities as shown in Figure 4-4 (a) – (d). The streamwise and vertical extent of these velocities beneath the block increased with higher Froude numbers. Thus, a zone of higher mean velocity compared to the respective free stream velocity indicates the reduced pressure zone increased with higher Froude number which means the ice block is more likely to be unstable with higher Froude number.

The increase in ice thickness-to-depth ratio (*t/h*) has a significant impact on the streamwise velocity. The contours show that larger *t/h* ratios caused more reduction in flow area resulting in increased mean velocity compared to the free stream velocity (Figure 4-4 (b), (e), (f)). Increasing the *t/h* ratio resulted in a longer and wider recirculation zone. The increase in estimated reattachment lengths with the increase in *t/h* is consistent with the previous investigation by Dow-Ambtman et al., (2011). This implies that an ice block with greater *t/h* ratios will cause a greater pressure reduction under the same approach flow conditions and is more likely to be unstable.

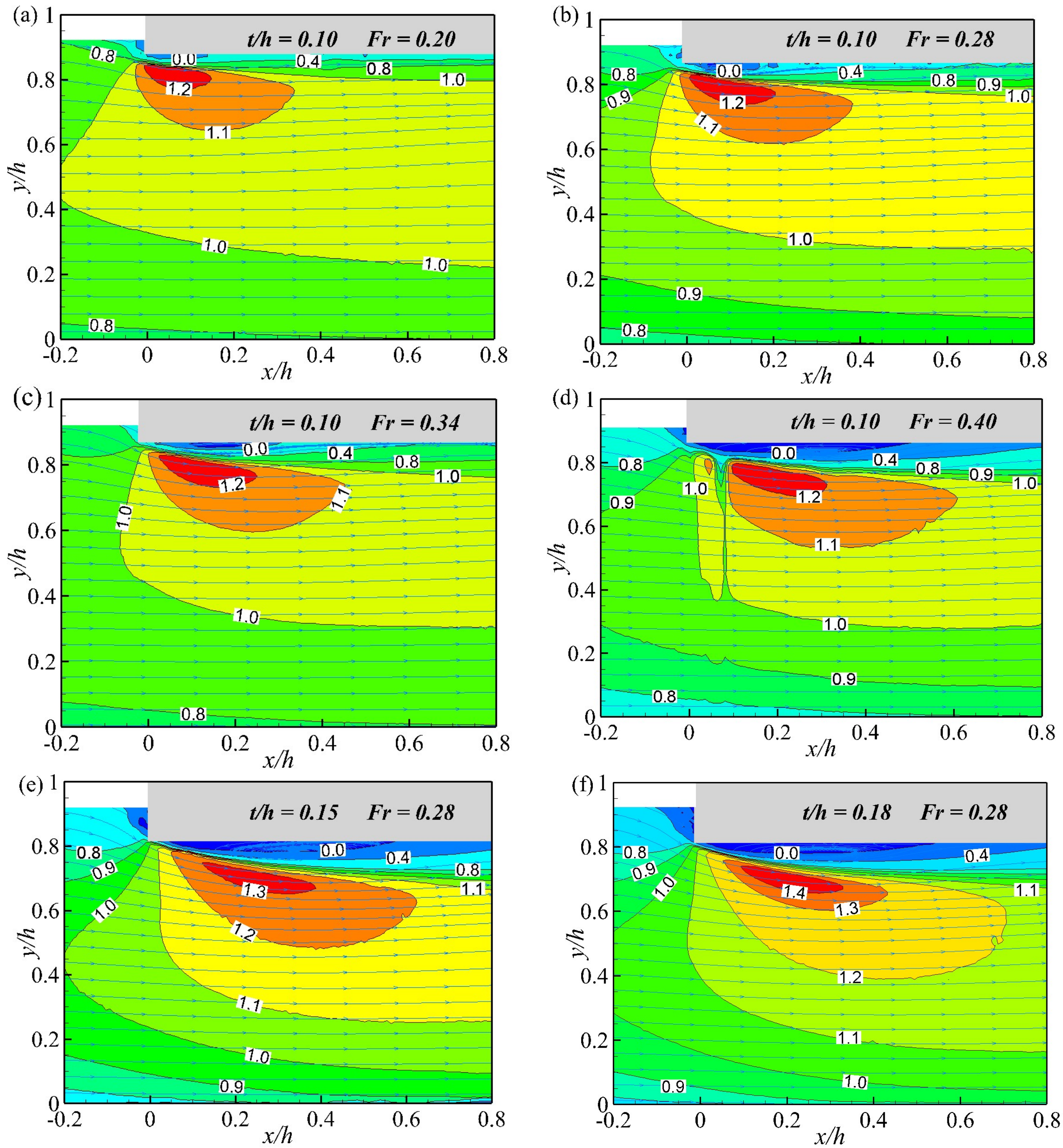

Figure 4-4: Contour plots of the normalized streamwise mean velocity ($U^* = U/U_e$) for various Froude numbers and thickness-to-depth ratios.

Contours of the normalized vertical mean velocities are shown in Figure 4-5. The flow is deflected downward at the leading edge of the block yielding high negative velocities at the leading edge, which is an indication of downward transport of flow. Beneath the ice block, positive vertical velocity indicates upward transport of flow close to the block. With increasing Froude numbers and *t/h* ratios, the zero-velocity contour observed to move downstream from the leading edge indicates a reduction of ice block stability with higher Froude number and *t/h* ratio. The areal extent of negative vertical velocity field increased from the vicinity of the leading edge both upstream and downstream and also towards the bottom of the channel with the increase in Froude number and *t/h* ratio. Thus, from this analysis, it can be concluded that if there is frazil ice present in the flow, deposition can occur further downstream from the leading edge with higher Froude numbers and greater *t/h* ratios.

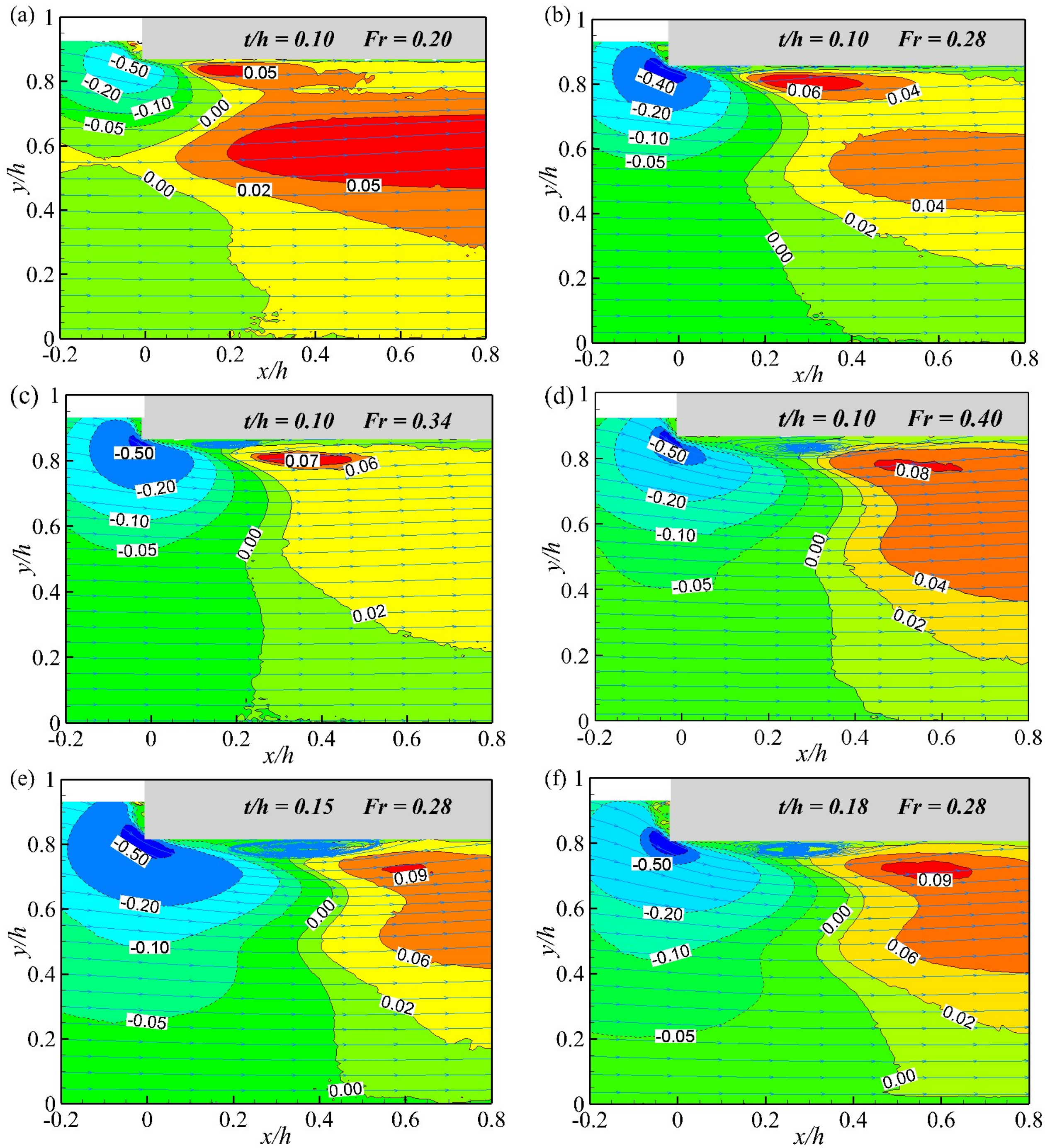

Figure 4-5: Contour plots of the normalized vertical mean velocity ($V^* = V/U_e$) for various Froude numbers and thickness-to-depth ratios.

4.3.2.2 Flow separation and reattachment length

The mean reattachment point was determined using three different techniques: the forward flow fraction method (defined as the fraction of time for which 50% of the flow directed in the downstream direction), zero mean velocity contour method (the *x*-location where the streamwise component of the mean velocity $U = 0$) and where the dividing streamline reattaches beneath the ice block. For all the Froude numbers and constant *t/h* ratio of 0.10, the calculated value of reattachment length (L_r) normalized by approach flow depth (h) are tabulated in Table 4-3. Results obtained for $F_r = 0.28$ were selected and compared to the experimental work of Ambtman (2009). Figure 4-6 shows that, for a constant *t/h* ratio, the reattachment length increases linearly with increasing Froude number. Table 4-4 shows the variation of reattachment length with *t/h* ratio. A higher *t/h* ratio separates the approach flow and deflects more which created a larger recirculation region. The results showed that reattachment length increased with the increase in *t/h* ratio which supports findings of Ambtman (2009).

Table 4-3. Reattachment length (L_r/h) for different Froude number for a fixed t/h ratio of 0.1.

Method	L_r/h $F_r = 0.20$	L_r/h $F_r = 0.28$	L_r/h $F_r = 0.34$	L_r/h $F_r = 0.40$
Forward flow fraction	0.15	0.18	0.32	0.5
Zero mean velocity contour	0.13	0.23	0.33	0.51
Dividing streamline reattachment	Not observed	0.19	0.31	0.53
Average	0.14	0.20	0.32	0.51

Table 4-4. Reattachment length (L_r/h) for different thickness-to-depth ratio at a fix Froude number of 0.28.

Method	L_r/h $t/h = 0.10$	L_r/h $t/h = 0.15$	L_r/h $t/h = 0.18$
Forward flow fraction	0.18	0.56	0.57
Zero mean velocity contour	0.23	0.56	0.57
Dividing streamline reattachment	0.19	0.49	0.60
Average	0.20	0.54	0.58

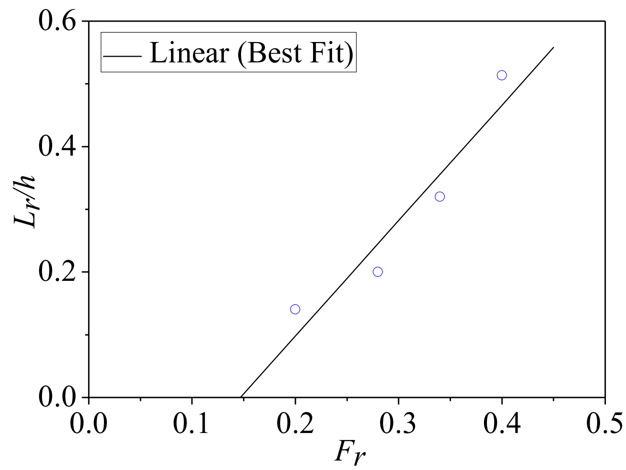

Figure 4-6. Variation of reattachment length with Froude number.

4.3.2.3 Mean velocity profiles

Figure 4-7 and Figure 4-8 represent the normalized profiles of streamwise velocity and vertical velocity for various Froude numbers and *t/h* ratios, respectively. The profiles were extracted at selected streamwise locations at x/L_r = 0, 0.5, 1, 2 and 3 considering x = 0 is at the leading edge of the ice block and L_r. Variation in Froude number and *t/h* ratio showed a significant effect on the normalized velocity profiles at the leading edge (x/L_r = 0), at the center of recirculation region (x/L_r = 0.5) and at the reattachment point (x/L_r = 1) beneath the ice block.

Figure 4-7(a) shows negative streamwise velocity at the leading edge and center of the recirculation region. It was observed that the vertical distance between the maximum negative velocity location and the ice block increases with the increase in Froude number. Figure 4-8 (a) shows that an increased t/h ratio caused a significant increase in the vertical distance between the maximum negative velocity location and the bottom of the ice block. However, beyond the recirculation region, the streamwise mean velocity for all Froude numbers are similar beyond $x/L_r = 3$ beneath the block. Beneath the separation zone, a thicker block under the same approach flow conditions causes greater flow constriction and increases flow acceleration. For all cases, streamwise velocity was observed to be higher than that of the free stream velocity near the leading edge up to the mid-depth of the channel from the ice block indicating that the presence of the ice block increased local flow velocity beneath the block in a channel. Further downstream from the reattachment point a more symmetric streamwise velocity distribution can be expected for all the cases in the present study.

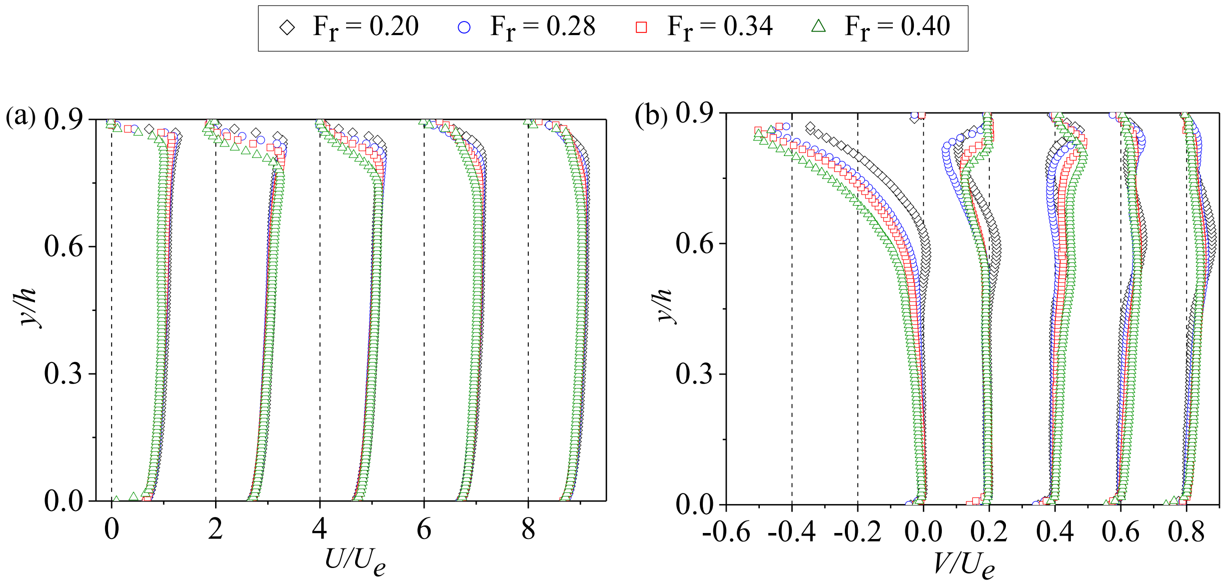

Figure 4-7: Normalized profiles of mean velocity (a) streamwise direction and (b) vertical direction beneath ice block at x/L_r = 0, 0.5, 1, 2, 3 where x = 0 is the edge of the ice block and L_r is the reattachment length for respective Froude number.

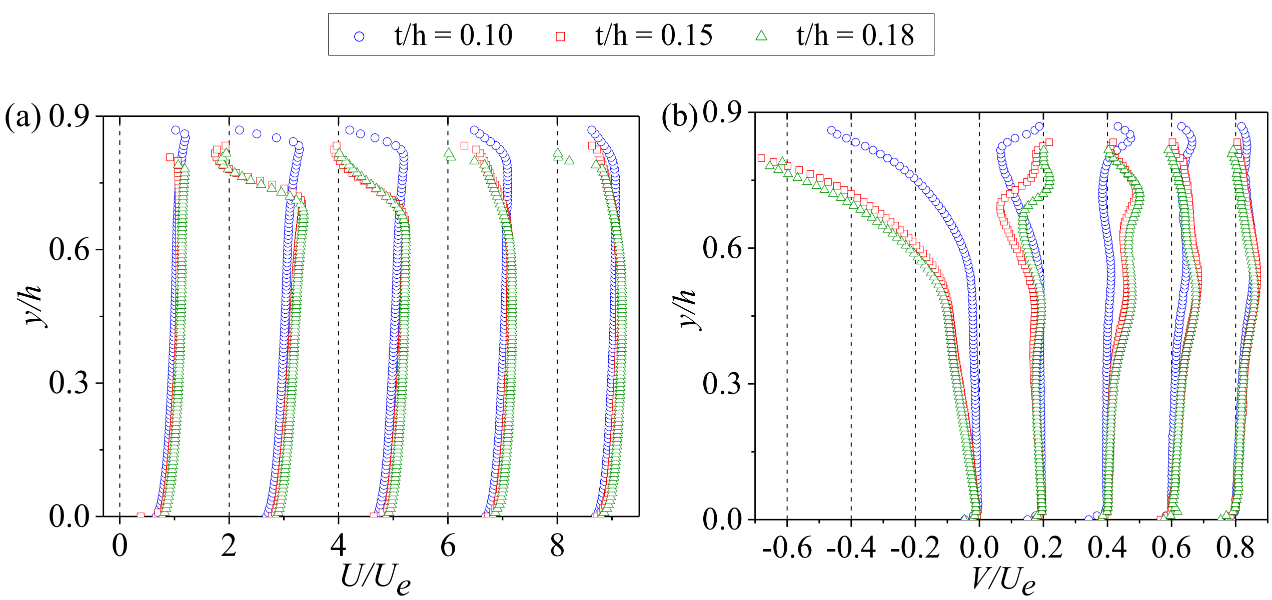

Figure 4-8: Normalized profiles of mean velocity (a) streamwise direction and (b) vertical direction beneath ice block at x/L_r = 0, 0.5, 1, 2, 3 where x = 0 is the edge of the ice block and L_r is the reattachment length for respective thickness-to-depth ratio.

Normalized profiles of vertical velocity for both Froude number variation (Figure 4-7 (b)) and *t/h* ratio variation (Figure 4-8 (b)) show negative vertical velocity at the leading edge and the center of recirculation region. Positive vertical velocity was observed at the reattachment point and after the reattachment. High negative velocity at the leading edge indicates downward vertical velocity and this downward vertical velocity increases with the increasing Froude number and *t/h* ratio suggests more instability can result from the larger separation bubble.

4.3.2.4 Maximum streamwise velocity location and magnitude

The position of the local maximum streamwise velocity beneath the ice block is presented in Figure 4-9. The sudden increase in maximum velocity occurred just after the flow passed the leading edge for all the cases, which can be attributed to the sudden reduction of pressure. The maximum velocity location below the block shifted downstream with the increase in the Froude number (Figure 4-9 (a)). The shift in data after x/h = 0.8 are not real but due to the two planes (Figure 4-9(a)). The highest *t/h* ratio caused the highest maximum velocity, which is consistent with the association of maximum low-pressure region with greater *t/h* ratios (Figure 4-9 (b)). As expected, the highest maximum velocity was observed near the leading edge of the block and afterward, the value of the maximum velocity decreased until it stabilized at a constant value beneath the block.

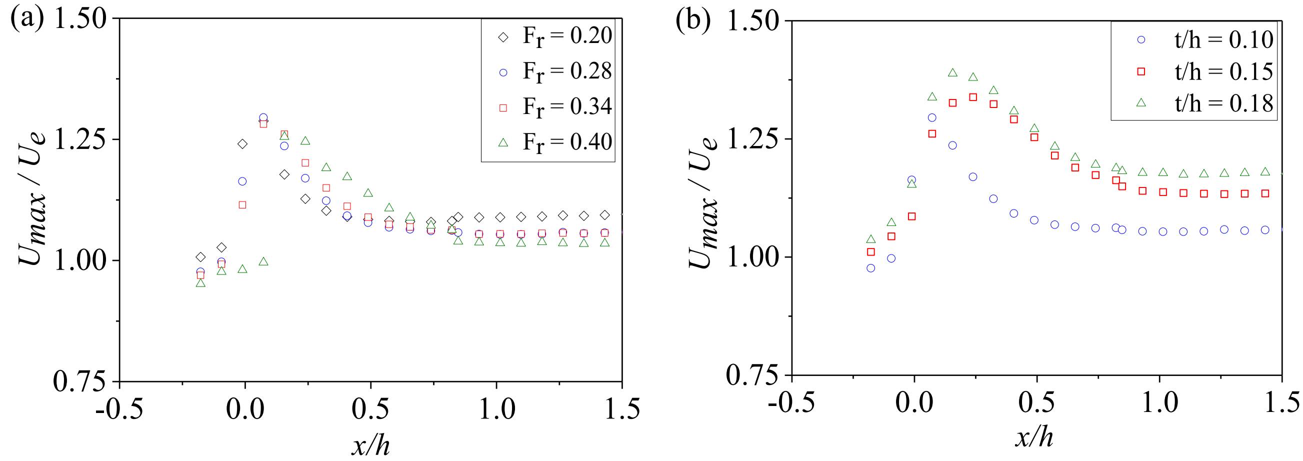

Figure 4-9: Streamwise maximum velocity locations for a) various Froude numbers b) various thickness-to-depth ratios.

4.3.2.5 Profiles of turbulence intensity

The effect of Froude number and *t/h* on turbulence intensity beneath the ice block are presented in Figure 4-10 and Figure 4-11respectively. The location of the profile extraction is the same as previous. The first location in the profiles for both streamwise (u') and vertical (v') direction is at the leading edge of the ice block. The presence of the ice block increased the turbulence intensity levels close to the ice block. Streamwise turbulence intensities are greater than the vertical turbulence intensities for both Froude number and *t/h* ratio experiments. For all cases, the highest value of turbulence intensity was observed within the recirculation region, which indicates the production of new energy-containing eddies within the recirculation zone. After reattachment, both the streamwise and vertical turbulence intensity for all the test cases decreased with the distance from the bed, reached a local minimum in the central region of the channel and then increased towards the block. The profiles are similar to the findings of turbulence intensity below simulated ice jams in the equilibrium region (Pahlavan, 2016) and turbulence intensity under a simulated smooth cover and rough bed (Parthasarathy & Muste, 1994) with the deviations occurring close to the top surface. As the greatest value of turbulence intensity is located near the ice block, the potential for the under surface erosion in this region could be high. An increase in Froude number and *t/h* ratio caused higher turbulence intensity within the recirculation region, but lower turbulence intensity after the reattachment both streamwise and vertical direction.

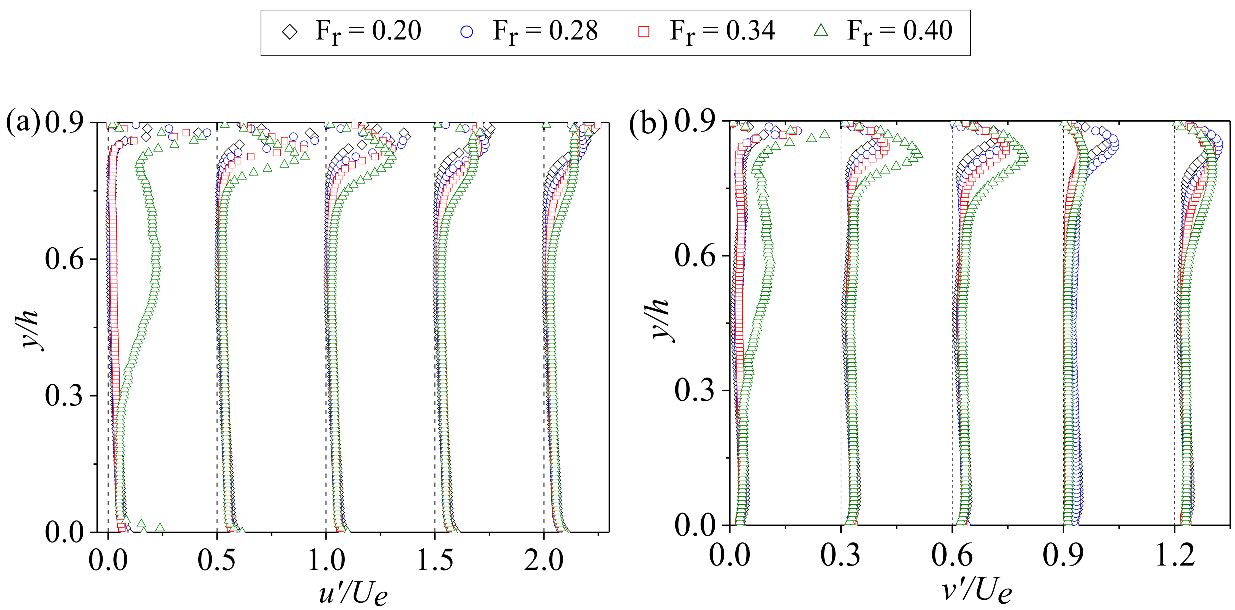

Figure 4-10: Normalized profiles of turbulence intensity (a) streamwise direction and (b) vertical direction beneath ice block at x/L_r = 0, 0.5, 1, 2, 3 where x = 0 is the edge of the ice block and L_r is the reattachment length for respective Froude number.

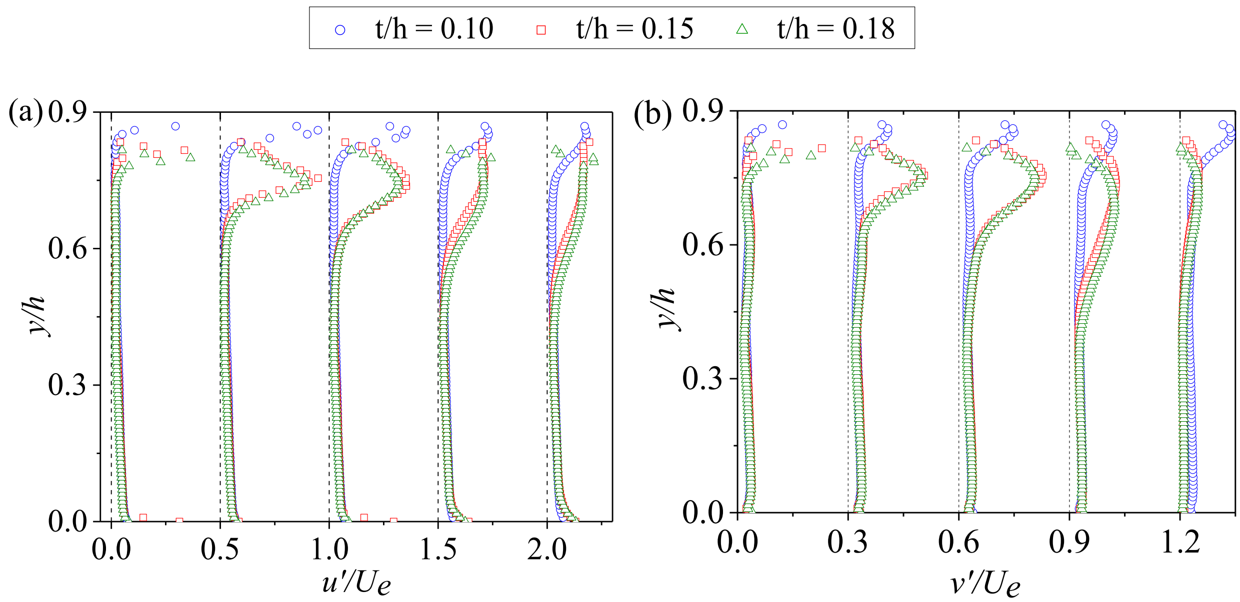

Figure 4-11: Normalized profiles of turbulence intensity (a) streamwise direction and (b) vertical direction beneath ice block at x/L_r = 0, 0.5, 1, 2, 3 where x = 0 is the edge of the ice block and L_r is the reattachment length for respective thickness-to-depth ratio.

4.3.2.6 Profiles of Reynolds shear stress

The profiles of Reynolds shear stress for the different Froude numbers and thickness-to-depth ratio (*t/h*) are presented in Figure 4-12 and Figure 4-13 respectively. A negative value of Reynolds shear stress was observed beneath the ice block, except at the leading edge where a positive value of Reynolds shear stress was observed. The negative $-\overline{uv}$ coincides with the positive contour locations of vertical velocity which indicates low momentum fluid moving to a region of high momentum beneath the ice block. This result showed similarity with the findings of Rifat (2017). The deposition is more likely to occur beneath the block after the reattachment region, as the flow with low momentum moving towards the high momentum at this location. A higher Froude number creates a greater value of $-\overline{uv}$ within the recirculation region beneath the ice block which also supports the large reattachment length observed from the streamlines in the mean velocity contour. The stresses were observed to decay after the flow passes the recirculation zone of the block, which can be attributed to the breakdown of large scale structures generated from flow separation at the leading edge of the block.

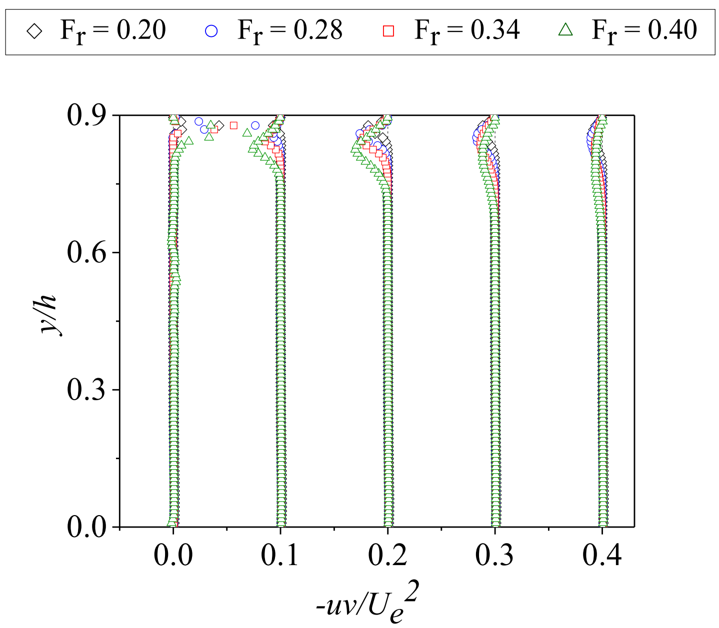

Figure 4-12: Normalized profiles of Reynolds shear stress beneath ice block at $x/L_r = 0, 0.5, 1, 2, 3$ where $x=0$ is the edge of the ice block and L_r is the reattachment length for respective Froude number.

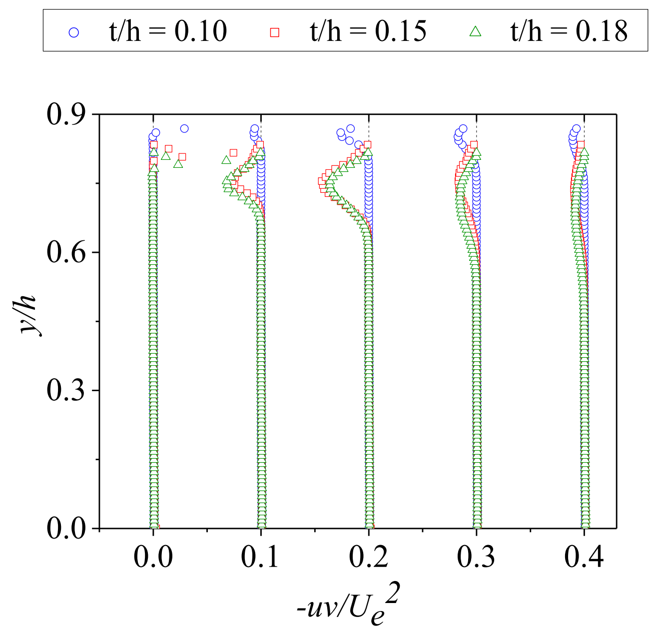

Figure 4-13: Normalized profiles of Reynolds shear stress beneath ice block at x/L_r = 0, 0.5, 1, 2, 3 where $x = 0$ is the edge of the ice block and L_r is the reattachment length for respective thickness-to-depth ratio.

4.3.2.7 Boundary shear stress

The presence of an ice block can influence the boundary shear stress both on the bed and beneath the ice block. In the present study, the shear velocity for different Froude numbers and various *t/h* ratios was determined using the Clauser plot method at a location further downstream from reattachment where the maximum velocity was not changing with the streamwise locations. Beneath the ice block, the log law was applied twice to each profile once from the bed and again from the ice block. The maximum velocity was considered as the dividing point of each profile. Shear stresses were then calculated from the shear velocity values. Figure 4-14 (a) was produced to examine the effect of Froude numbers on boundary shear stress beneath the ice block (τ_i) and at the channel bed (τ_b). It was observed that the presence of ice block increases boundary shear stress at both boundaries with the increase in Froude number. The present findings corroborate results from previous studies on shear stress along the wall of a pipe by Ahsan (2014) and bed shear stress during breakup by Zare et al., 2016. As expected, greater *t/h* ratio reduces the effective flow area and increases flow velocity and boundary shear stress both beneath the ice block and on the channel bed (Figure 4-14 (b)).

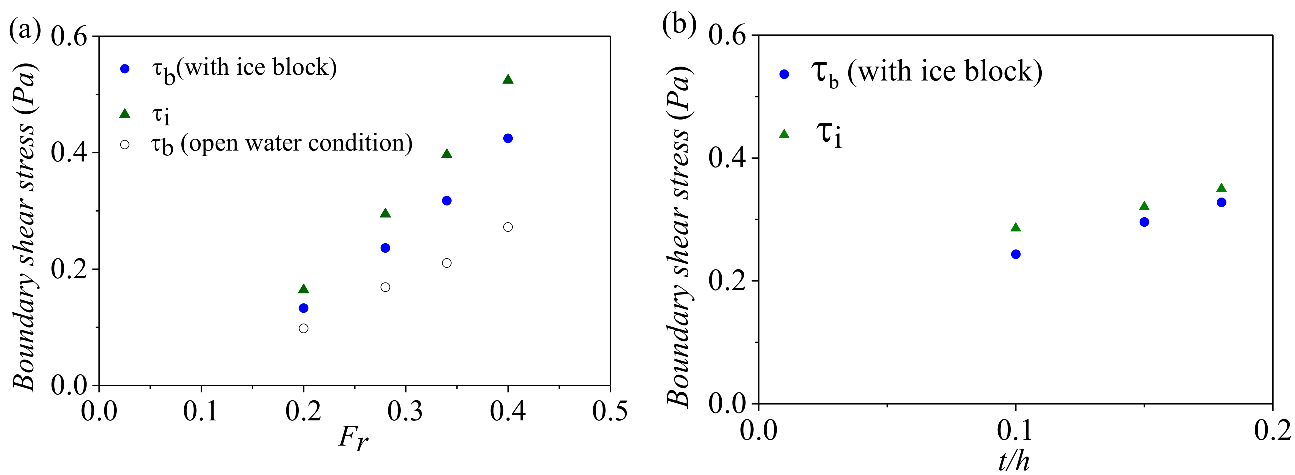

Figure 4-14: Variation of boundary shear stress for a) various Froude numbers b) various thickness-to-depth ratios.

4.4 Conclusions

An experimental study was conducted to investigate the effects of Froude numbers and *t/h* ratios on the velocity field beneath an ice block. A range of Froude numbers ($0.20 \leq F_r \leq 0.40$) were tested keeping the *t/h* ratio of the block constant at 0.10. Similarly, a range of *t/h* ratios (0.10, 0.15, 0.18) were tested keeping the Froude number constant at 0.28. The results showed that the presence of an ice block causes a redistribution of flow from beneath the block towards the bed of the channel with *t/h* having the greatest impact on flow redistribution. This was due to the greater reduction of flow area and increased flow separation at the leading edge. With respect to frazil accumulation, the negative vertical velocity near the leading edge and positive vertical velocity beneath the ice block indicates frazil, if present, would be more likely to suspend beneath the block closer to the leading edge and would be more likely to deposit beneath the block after the reattachment point. The analysis revealed that the reattachment length increased linearly from L_r/h = 0.14 to 0.51 with the increase in the Froude number from 0.20 to 0.40. For the *t/h* ratio test, L_r/h increased for a greater *t/h* ratio. The significant increase in the recirculation region for both higher Froude number and greater *t/h* ratio caused higher pressure reduction beneath the ice block at the leading edge. The Reynolds shear stress for higher Froude number and greater *t/h* ratios indicates high momentum transport downward at the edge of the ice block. Boundary shear stress has practical implications for the transport of sediment and frazil ice. With higher Froude numbers and *t/h* ratios, there would be an increased tendency of boundary shear stress beneath the block and on the bed which can cause erosion beneath the block and channel bed and also can reduce the ice block stability.

This study represents a good first step in attempting to further our understanding of the effects of Froude number and ice thickness-to-depth ratio on the velocity field beneath the ice block. There are still, however, many potential future areas of research to explore that will strengthen and deepen our knowledge on the topic. Future researchers should consider the effect of different parameter sets, such as the channel aspect ratio, cross-sectional geometry, roughness of the bed and ice cover, a wide range of *t/h* ratio to enhance the existing knowledge on this field.

4.5 References

Ahsan, M. (2014). Numerical analysis of friction factor for a fully developed turbulent flow using k e ε turbulence model with enhanced wall treatment. *Journal of Basic and Applied Sciences*, *3*(4), 269–277.

Akon, A. F. (2017). *Effects of turbulence on the separating-reattaching flow above surface-mounted, three-dimensional bluff bodies*. PhD thesis. Mechanical and Materials Engineering. The University of Western Ontario.

Ambtman, K. E. D. (2009). *Experimental Investigation of Ice Floe Stability*. Ph.D. Thesis, Department of Civil and Environmental Engineering, University of Alberta, Edmonton, Alberta.

Ashton, G.D. (1974). Froude criterion for ice-block stability. *Journal of Glaciology*. 13(68), 307-313.

Casarsa, L. & Giannattasio, P. (2008) Three-dimensional features of the turbulent flow through a planar sudden expansion. *Physics of Fluids*, 20 (1), 015103.

Coleman, H. W., & Steele, W. G. (1995). Engineering application of experimental uncertainty analysis. *AIAA Journal*, 33, 1888-1896.

Coutermarsh, B & McGilvary, R. (1994). Analyzing the stability of floating ice floes. CRREL Report. 94-13.

Daly, S.F. & Axelson, K.D. (1990). Stability of floating and submerged blocks. *Journal of Hydraulic Research*, 28(6), 737-752.

Dow-Ambtman, K. E., Hicks, F. E., & Steffler, P. M. (2011). Experimental Investigation of the Pressure Distribution beneath a Floating Ice Block. *Journal of Hydraulic Engineering*, 137(4), 399–411.

Dow-Ambtman K. E., Steffler P. M., & Hicks F. E. (2011). Analysis of the stability of floating ice blocks. *Journal of Hydraulic Engineering*. 137(4), 412-422.

Forliti, D. J., Strykowski, P. J., & Debatin, K. (2000). Bias and precision errors of digital particle image velocimetry. *Experiment in Fluids*, 28, 436-447.

Jasek, M. (2003). Ice jam release and break-up front propagation. *Proceedings of the 12th workshop on the hydraulics of ice covered rivers, The CGU HS Committee on River Ice Processes and the Environment*. June 19-20, 2003, Edmonton, AB, 348-368.

Larsen, P. (1975). Notes on the stability of floating ice blocks. *Proceedings of the IAHR third international symposium on ice problems*. Hanover, NH, IAHR, 305-313.

Nezu, I. & Nakagawa, H. (1993). Turbulence in Open-Channel Flows. CRC Press, Taylor &. Francis Group.

Pahlavan, H. (2016). An Experimental Investigation of Turbulent Flow Characteristics Beneath an Ice Jam. M. Sc. Thesis. Department of Civil Engineering, University of Manitoba, Winnipeg, Manitoba.

Parthasarathy, R.N. & Muste, M. (1994). Velocity measurements in asymmetric turbulent channel flows. *Journal of Hydraulic Engineering,* 120 (9), 1000 –1020.

Prasad, A. K., Adrian, R. J., Landreth, C. C. & Offutt, P. W. (1992). Effect of resolution on the speed and accuracy of particle image velocimetry interrogation. *Experiments in Fluids*, 13, 105-116.

Rifat, S. M. (2017). *Effects of Wall Roughness over Forward Facing Step in Open Channel Turbulent Flow*. Department of Mechanical Engineering, University of Manitoba, Winnipeg, Manitoba.

Rona, A. & Grottadaurea, M. (2010). Generalized Coles' law and outer layer conformal mapping. Journal of Hydraulic Research, 48 (5), 674-679.

Singh, A. (2013). *Studies on variation of boundary layer parameters on rough surfaces in turbulent boundary layer zone.* Master of Technology thesis, Department of Civil Engineering, National Institute of Technology, Rourkela.

Shah, M. K., & Tachie, M. F. (2008). PIV study of turbulent flow in asymmetric converging and diverging channels. *Journal of Fluids Engineering*, 130 (1), 011204 (1-15).

Sherry, M., Lo Jacono, D., & Sheridan, J. (2010). An experimental investigation of the recirculation zone formed downstream of a forward facing step. *Journal of Wind Engineering and Industrial Aerodynamics*, *98*(12), 888–894.

Uzuner, M.S. & Kennedy, J.F. (1972). Stability of floating ice blocks. *Journal of the Hydraulics Division*, 98 (HY12), 2117-2133.

Chapter 5 : **CONCLUSIONS AND RECOMMENDATION**

5.1 Conclusions

This research attempted to understand the flow dynamics beneath an ice block through a series of experiments using particle image velocimetry. An approaching ice block can cause the upstream progression of an ice cover if it comes to rest at the edge of intact ice cover or it can become entrained which can thicken the ice cover or potentially weaken it depending on the impact of the block. This can have an impact on ice jam formation dynamics as well as release. Previous studies suggested the importance of localized flow behavior due to flow separation and acceleration on the resulting stability of the ice block. Thus the objective of this research was to characterize the velocity field beneath an ice block. The effects of two normalized parameters with different magnitude were assessed in the course of the research; the first parameter was Froude number and the second parameter was the ice thickness-to-depth of flow (*t/h* ratio). For the Froude number experiments, a range of Froude numbers ($0.20 \leq Fr \leq 0.40$) were tested keeping the *t/h* ratio of the block constant and for *t/h* ratio experiments, various ratios (0.10, 0.15, 0.18) were examined with a constant Froude number.

The contours of the mean velocities both in streamwise and vertical direction showed that the presence of an ice block causes a redistribution of flow beneath the ice covered section for the change in both parameters. Increased flow separation at the leading edge was observed with the increase in the Froude number and *t/h* ratio. The negative vertical velocity near the leading edge of the ice block and the positive vertical velocity below the ice block were observed to increase with increasing Froude number and *t/h* ratio. This indicates ice block will experience a higher submerging force with the increase in the Froude number and *t/h* ratio. The analysis revealed that the reattachment length increased linearly from L_r/h = 0.14 to 0.51 with the increase in the Froude number from 0.20 to 0.40. L_r/h also increased for a greater *t/h* ratio. The significant increase in the recirculation region for both higher Froude number and greater *t/h* ratio causes a higher pressure reduction beneath the ice block at the leading edge. A higher value of Reynolds shear stress was observed within the recirculation region for all Froude number and *t/h* ratio experiments. With higher Froude numbers and *t/h* ratios, there would be an increased tendency of boundary shear stress beneath the block and on the bed.

This study represents a good first step in attempting to further our understanding of the effects of Froude number and ice thickness-to-depth ratio on the flow distribution beneath a floating ice block.

5.2 Recommendations

Particle image velocimetry was found to be an effective non-intrusive velocity measurement technique beneath an ice block. Although this research studied the turbulent flow beneath an ice block for the first time, there are still many opportunities to improve this study and to enhance the existing knowledge on this field. A list of possible future research is presented as follows:

1. For future work, the scaling of the experiment can be improved, as the current experimental facility does not allow flow with higher Froude numbers and higher *t/h* ratios than the present study.
2. Further, quantify the effects of different Froude numbers and *t/h* ratios by increasing the range of Froude numbers and *t/h* ratios.
3. The potential of the PIV technique could utilize to observe the velocity field beneath the block for flow with different angles of attack at the leading edge.
4. The future experiment can be done using different Froude numbers and *t/h* ratios by changing the leading edge shape of the ice block.
5. Quantify the effect of cross-sectional geometry (e.g. trapezoidal channel) on the velocity field beneath the ice block.
6. Future research can be done by changing the roughness of the bed and beneath the ice block.
7. Future analysis can be extended to study the effects of Froude numbers and *t/h* ratios on the velocity field in the recovery regions beneath the ice block.
8. Future study can be carried out to study the turbulent flow features over an entire cross-section at different locations beneath the ice block using 3D particle image velocimetry since the instrument can measure three components of flow velocity in a volume of fluid.
9. This technique could be used to understand the dynamics of ice jam thickening or ice jam progression.
10. Lastly, the results of the present study can be used to validate numerical turbulence models related to river ice studies.

REFERENCES

Ahsan, M. (2014). Numerical analysis of friction factor for a fully developed turbulent flow using k e ε turbulence model with enhanced wall treatment. *Journal of Basic and Applied Sciences*, *3*(4), 269–277.

Akon, A. F. (2017). *Effects of turbulence on the separating-reattaching flow above surface-mounted, three-dimensional bluff bodies*. PhD thesis. Mechanical and Materials Engineering. The University of Western Ontario.

Ambtman, K. E. D. (2009). *Experimental Investigation of Ice Floe Stability*. Ph.D. Thesis, Department of Civil and Environmental Engineering, University of Alberta, Edmonton, Alberta.Ashton, G.D. (1974). Froude criterion for ice-block stability. *Journal of Glaciology*. 13 (68), 307-313.

Beltaos, S., Carter, T., & Rowsell, R. (2012). Measurements and analysis of ice breakup and jamming characteristics in the Mackenzie Delta, Canada. *Cold Regions Science and Technology*, *82*, 110–123. https://doi.org/10.1016/j.coldregions.2012.05.013

Casarsa, L. & Giannattasio, P. (2008) Three-dimensional features of the turbulent flow through a planar sudden expansion. *Physics of Fluids*, 20 (1), 015103.

Chow, V.T. (1959). *Open-Channel Hydraulics*. New York, USA: McGraw-Hill Book Company.

Coleman, H. W., & Steele, W. G. (1995). Engineering application of experimental uncertainty analysis. *AIAA Journal*, 33, 1888-1896.

Coles, D. (1956). The law of the wake in the turbulent boundary layer. *Journal of Fluid Mechanics*, 1(2), 191-226.

Coutermarsh, B & McGilvary, R. (1994). Analyzing the stability of floating ice floes. CRREL Report. 94-13.

Daly, S.F. & Axelson, K.D. (1990). Stability of floating and submerged blocks. *Journal of Hydraulic Research*, 28(6), 737-752.

Dow-Ambtman, K. E., Hicks, F. E., & Steffler, P. M. (2011). Experimental Investigation of the Pressure Distribution beneath a Floating Ice Block. *Journal of Hydraulic Engineering*, 137(4), 399–411.

Dow-Ambtman K. E., Steffler P. M., & Hicks F. E. (2011). Analysis of the stability of floating ice blocks. *Journal of Hydraulic Engineering*. 137(4), 412-422.

Forliti, D. J., Strykowski, P. J., & Debatin, K. (2000). Bias and precision errors of digital particle image velocimetry. *Experiment in Fluids*, 28, 436-447.

Gerard, R. (1980). Flow in ice covered channels: Some fundamentals. *Proceedings of Workshop on Hydraulic Resistance of River Ice: Canada Centre for Inland Waters*, Burlington, Ontario.

Jasek, M. (2003). Ice jam release and break-up front propagation. *Proceedings of the 12th workshop on the hydraulics of ice covered rivers, The CGU HS Committee on River Ice Processes and the Environment*. June 19-20, 2003, Edmonton, AB, 348-368.

Keulegan, G.H. (1938). Laws of Turbulent Flow in Open Channels. *Journal of Research of the National Bureau of Standards*, 707-741.

Larsen, P. (1975). Notes on the stability of floating ice blocks. *Proceedings of the IAHR third international symposium on ice problems*. Hanover, NH, IAHR, 305-313.

Lau, Y.L. (1982). Velocity distributions under floating covers. *Canadian Journal of Civil Engineering*, 9 (1), 76-83.

Nezu, I. & Nakagawa, H. (1993). Turbulence in Open-Channel Flows. CRC Press, Taylor &. Francis Group.

Nyantekyi-Kwakye, B. (2016). *Experimental Investigation on the Flow Characteristics of Three-Dimensional Turbulent Offset Jets*. Ph.D. Thesis, Department of Mechanical Engineering, University of Manitoba, Winnipeg, Manitoba.

Nyantekyi-kwakye, B., Clark, S. P., Dow, K., & Tachie, M. F. (2017). Investigating Turbulent Flow Characteristics beneath a Simulated Ice Jam Using Particle Image Velocimetry. *CGU HS Committee on River Ice Processes and the Environment*. July 9-12, 2017, Whitehorse, Yukon, Canada.

Pahlavan, H. (2016). *An Experimental Investigation of Turbulent Flow Characteristics Beneath an Ice Jam*. M. Sc. Thesis. Department of Civil Engineering, University of Manitoba, Winnipeg, Manitoba.

Parthasarathy, R.N. & Muste, M. (1994). Velocity measurements in asymmetric turbulent channel flows. *Journal of Hydraulic Engineering,* 120 (9), 1000 –1020.

Prasad, A. K., Adrian, R. J., Landreth, C. C. & Offutt, P. W. (1992). Effect of resolution on the speed and accuracy of particle image velocimetry interrogation. *Experiments in Fluids*, 13, 105-116.

Raffel, M., Willert, C. E. & Kompenhans, J., 1998. *Particle Image Velocimetry: A Practical Guide.* 3 ed. Berlin: Springer.

Rifat, S. M. (2017). *Effects of Wall Roughness over Forward Facing Step in Open Channel Turbulent Flow*. M. Sc. Thesis. Department of Mechanical Engineering, University of Manitoba, Winnipeg, Manitoba.

Rona, A. & Grottadaurea, M. (2010). Generalized Coles' law and outer layer conformal mapping. Journal of Hydraulic Research, 48 (5), 674-679.

Robert, A., & Tran, T. (2012). Mean and turbulent flow fields in a simulated ice-covered channel with a gravel bed: some laboratory observations. *Earth surface Processes and Landforms,* 37(9), 951–956.

Shah, M. K., & Tachie, M. F. (2008). PIV study of turbulent flow in asymmetric converging and diverging channels. *Journal of Fluids Engineering*, 130 (1), 011204 (1-15).

Sherry, M., Lo Jacono, D., & Sheridan, J. (2010). An experimental investigation of the recirculation zone formed downstream of a forward facing step. *Journal of Wind Engineering and Industrial Aerodynamics*, *98*(12), 888–894.

Singh, A. (2013). *Studies on variation of boundary layer parameters on rough surfaces in turbulent boundary layer zone.* Master of Technology thesis, Department of Civil Engineering, National Institute of Technology, Rourkela.

Teal, M. J., Ettema, R., & Walker, J. F. (1994). Estimation of mean flow velocity in ice-covered channels. *Journal of Hydraulic Engineering*, 120(12), 1385–1400.

Uzuner, M.S. & Kennedy, J.F. (1972). Stability of floating ice blocks. *Journal of the Hydraulics Division*, 98 (HY12), 2117-2133.

Westerweel, J., Draad, A. A., van der Hoeven, Th. J. G. and van Oord, J. (1996). Measurement of Fully Developed Turbulent Pipe Flow with Digital Particle Image Velocimetry. *Experiments in Fluids*, 20, 165-177.

Walker, J. F., & Wang, D. (1997). Measurement of flow under ice covers in North America. *Journal of Hydraulic Engineering*, 123(11), 1037–1040.

Yamaguchi, H., & Hirayama, K. (1990). Measurements of flow velocity under the ice cover. *IAHR Ice Symposium,* 1155-1170.

Zhang, C., Vasilevskis, S. & Kozlowski, B., 2018. *Particle Image Velocimetry: User Guide,* Aalborg, Denmark: Aalborg University: Department of Civil Engineering.

Zhao, X., Lian, J. jian, & Song, X. yan. (2017). Analyses of the stability of submerged ice blocks. *Journal of Hydrodynamics*, *29*(3), 460–469. https://doi.org/10.1016/S1001-6058(16)60757-6

Zufelt, E., & Ettema, R. (1997). Unsteady Ice Jam Processes. CRREL Report 97-7, U.S. Army Cold Regions Research and Engineering Laboratory.

APPENDIX: MEASUREMENT UNCERTAINTY

A complete uncertainty analysis of the velocity measurements using PIV is presented in this appendix.

Measurement error

Measurement error is the difference between the measured value and the true value of the parameter. Due to the inherent limitations of the measurement system and procedure, measurement error cannot be avoided and uncertainty analysis is used to quantify the error. In general, the total error is made up of two major components; a precision (random) error (*P)* and a bias (systematic) error (*B)*. An error is classified as precision if it is contributed by the scatter of the measured data; otherwise, it is a bias error. The bias error (also known as the systematic error) is associated with the error introduced by the measurement system and procedure, such as the camera resolution and the calibration of the field of view. In other words, the bias error always occurs with the same value, when the measurement system and procedure remain the same. With the PIV technique, measurement errors can be introduced by seeding particles, sub-pixel displacement bias, insufficient sample size, particle response to fluid motion, laser sheet positioning, the effect of velocity gradient, etc. Coleman and Steele, 1995 presented a detailed uncertainty assessment methodology following the AIAA standard and this employed in the present study.

In the present study, precautionary measures were taken to minimize errors in data acquisition and post-processing. For example, the settling velocity and response time of the seeding particles were calculated and results confirmed that the particles followed the flow faithfully. The laser sheet was carefully aligned to the centerline of the test channel to reduce any possible errors from light sheet positioning. The time between two successive pulses of the laser was set such that the maximum particle displacement was less than 1/4 of the interrogation area size used. The interrogation area (32 pixels × 32 pixels with 50% overlap in both the x and y directions) was chosen to be small as possible to contain a sufficient number of particles and also improve spatial resolution. In the present study, an adaptive correlation algorithm with a one-dimensional Gaussian peak-fitting function was used to determine the average particle displacement within the interrogation window to sub-pixel accuracy. The adaptive correlation algorithm is an advanced form of cross-correlation algorithm which uses a multi-pass fast Fourier transform. Precautionary measures were taken to minimize peak locking in image processing. Another major contributor to bias error is peak locking. In order to minimize the errors associated with peak locking, steps need to be taken during image acquisition and processing. Raffel et al. (1998) recommended that to reduce peak locking, the particle image diameter should be close to 2.0 pixels. The large sample size (8000 instantaneous images) used in the computation of the statistics in the present study also minimized the precision error.

Bias error

In PIV measurements, the instantaneous velocity, U_i at a given location in an average velocity field is calculated as follows;

$$U_i = \frac{\Delta s \, L_0}{\Delta T \, L_1} \qquad \text{A.1}$$

Where, Δs is the particle displacement, Δt is the time between the two laser pulses, L_0 and L_1 are the widths of the camera view in the object plane and the digital image respectively.

To determine the associated bias error, the root-sum-squares (RSS) of the elementary bias limits based on the sensitivity coefficients given in Eq. (A.2) is utilized

$$B_{U_i}^2 = \eta_{\Delta s}^2 B_{\Delta s}^2 + \eta_{L_0}^2 B_{L_0}^2 + \eta_{\Delta T}^2 B_{\Delta T}^2 + \eta_{L_1}^2 B_{L_1}^2 \quad \text{A.2}$$

Based on the equations provided, the bias errors were performed for U and V for the various test conditions and locations. A typical case has been presented in Tables A.1 and A.2. The percentage bias error (%Bias error) for both U and V cases are expressed as a percentage of U.

Table A.1: Bias limits of the local streamwise mean velocity (*U*) at *x*/*h* =0 and *y*/*h* =0.8 below the ice block.

Variable	**Magnitude**	**B**	**η**	**Bη**	**(Bη)²**
L_0 (m)	1.33E-01	5.00E-04	3.14E+00	1.57E-03	2.47E-06
L_1 (pix)	2.05E+03	5.00E-01	2.04E-04	1.02E -04	1.04E-08
Δt(s)	1.94E-03	1.00E-07	2.15E+02	2.15E-05	4.64E-10
Δs (pix)	1.25E+01	1.27E-02	3.35E-02	4.25E-04	1.81E-07
U (m/s)	4.18E-01				
				$\sum(B\eta)^2$	2.66E-06
				Bias error	1.63E-03
				% Bias error	0.39%

Table A.2: Bias limits of the local vertical mean velocity (V) at *x/h* =0 and *y/h* =0.8 below the ice block.

Variable	Magnitude	B	η	Bη	(Bη)²
L_0 (m)	1.33E-01	5.00E-04	-1.47E+00	-7.33E-04	5.37E-07
L_1 (pix)	2.05E+03	5.00E-01	-9.52E-05	-4.76E-05	2.26E-09
Δt(s)	1.94E-03	1.00E-07	-1.00E+02	-1.00E-05	1.01E-10
Δs (pix)	5.82E+00	1.27E-02	-3.35E-02	-4.25E-04	1.81E-07
U (m/s)	-1.95E-01				
				$\sum(B\eta)^2$	7.20E-07
				Bias error	8.48E-04
				% Bias error	0.20%

Precision error

The precision error, *P* is estimated as

$$P \quad \frac{T\sigma}{\sqrt{N}} \qquad \text{A.3}$$

where *T* is the confidence coefficient, *N* is the sample size =8000 and *σ* is the standard deviation. For a 95% confidence level, *T* has a value of 2 as suggested by Holman (2001). To calculate the standard deviation, *σ*, the sample size (8000 image pairs) used in the present study was subdivided into 10 sets and each set was used to calculate the mean velocities. The values of *U* and *V* were determined at the same locations of the flow. From the 10 sub-datasets, the standard deviation for *U* and *V* was approximately and respectively. With known values of *T, N* and *σ*, the precision error was estimated from Eqn. (A.3) to be approximately 0.04% and 0.05% for *U* and *V* respectively. Due to the large sample size used in the present, the precision error is negligible.

Total error

The total uncertainty, E is defined as the RSS of the bias and precision errors as

$$E = \sqrt{B^2 + P^2} \qquad \text{A.4}$$

The total uncertainty was calculated from the bias and precision errors obtained earlier to be 0.39% and 0.21% for U and V, respectively.

Following the suggestion by Casarsa and Giannattasio (2008), compared to the turbulent fluctuations, the effects of measurement errors on the higher-order statistics are negligible due to the averaging procedure for the random errors. However, the sampling error induced by the limited number of samples must be evaluated. Following Casarsa and Giannattasio (2008), the sampling errors of second-order statistics can be computed as

$$E_{u'} = \frac{T}{\sqrt{2N}} \qquad \text{A.5}$$

$$E_{-u} = \frac{T}{\sqrt{N}} \qquad \text{A.6}$$

The uncertainty in the turbulence intensities and Reynolds stresses were obtained as 1.55% and 2.19% respectively.